

Glacial Meltwater Identification in the Amundsen Sea

LOUISE C. BIDDLE, KAREN J. HEYWOOD, AND JAN KAISER

*Centre for Ocean and Atmospheric Sciences, School of Environmental Sciences, University of East Anglia,
Norwich, United Kingdom*

ADRIAN JENKINS

British Antarctic Survey, Cambridge, United Kingdom

(Manuscript received 10 October 2016, in final form 1 February 2017)

ABSTRACT


Pine Island Ice Shelf, in the Amundsen Sea, is losing mass because of warm ocean waters melting the ice from below. Tracing meltwater pathways from ice shelves is important for identifying the regions most affected by the increased input of this water type. Here, optimum multiparameter analysis is used to deduce glacial meltwater fractions from water mass characteristics (temperature, salinity, and dissolved oxygen concentrations), collected during a ship-based campaign in the eastern Amundsen Sea in February–March 2014. Using a one-dimensional ocean model, processes such as variability in the characteristics of the source water masses on shelf and biological productivity/respiration are shown to affect the calculated apparent meltwater fractions. These processes can result in a false meltwater signature, creating misleading apparent glacial meltwater pathways. An alternative glacial meltwater calculation is suggested, using a pseudo–Circumpolar Deep Water endpoint and using an artificial increase in uncertainty of the dissolved oxygen measurements. The pseudo–Circumpolar Deep Water characteristics are affected by the under ice shelf bathymetry. The glacial meltwater fractions reveal a pathway for 2014 meltwater leading to the west of Pine Island Ice Shelf, along the coastline.

1. Introduction

The West Antarctic Ice Sheet holds up to 3.3 m of potential sea level rise (Bamber et al. 2009) and has been observed to contain some of the fastest thinning ice shelves around Antarctica, with up to 7 m a^{-1} thinning (Pritchard et al. 2012). One of the largest sources of glacial meltwater (MW), a component of which is associated with this thinning, is the Amundsen Sea Embayment in Antarctica (Rignot et al. 2013), particularly Pine Island Ice Shelf (PIIS). This region is undergoing oceanic melting, where the warm Circumpolar Deep Water (CDW) is able to access the grounding line of the ice shelves and melt the ice from below (Jacobs et al. 1996; Payne et al. 2004; Jacobs et al. 2012). Most model studies and observations have focused on identifying the

drivers for the transport of the CDW to the ice shelves, which is an important process for modeling future glacial melting and sea level rise (Jacobs et al. 2012; Jenkins et al. 2016). Here we focus on the identification of MW traveling away from the ice shelf.

Observations and model results from around Antarctica show that understanding the fate of the MW is essential in order to improve global climate models and forecast future climate scenarios better (IPCC 2014). Potential impacts of increased MW input include slow down of Antarctic Bottom Water (AABW) formation, with consequential effects on the global meridional overturning circulation and changes to sea ice formation rates (Richardson et al. 2005). Some of these effects have already begun to be observed, most distinctly in the freshening of the Ross Sea shelf waters (Jacobs and Giulivi 2010). This freshening has been attributed to West Antarctic Ice Sheet melt, particularly from the

 Denotes content that is immediately available upon publication as open access.

Corresponding author e-mail: Louise C. Biddle, louise.biddle@uea.ac.uk



This article is licensed under a Creative Commons Attribution 4.0 license (<http://creativecommons.org/licenses/by/4.0/>).

Amundsen Sea region, traveling west to the Ross Sea in the Antarctic Coastal Current (Jacobs and Giulivi 2010; Nakayama et al. 2014). However, because of uncertainties associated with MW identification, the pathway of glacial meltwater from any of the Amundsen Sea ice shelves has not been observed beyond the Amundsen Sea Embayment (Nakayama et al. 2013; Randall-Goodwin et al. 2015; Kim et al. 2016).

The Amundsen Sea has three main water masses: modified CDW (mCDW), Winter Water (WW), and Antarctic Surface Water (AASW). The mCDW and WW are identified as the salinity maximum and temperature minimum (below the surface), respectively. Once the CDW has traveled onto the continental shelf, it is referred to as modified CDW and is typically 2° – 4° C above the in situ freezing temperature (Dutrieux et al. 2014). The WW lies above the mCDW in the water column and is formed seasonally through heat loss to the atmosphere affecting the temperature and sea ice formation affecting the salinity. AASW is observed in the austral summer and is heated through solar radiation and freshened through sea ice melt. PIIS is melted primarily by the warm mCDW, and so the MW will mix with this water mass (Jenkins 1999). Because of the low content of MW that is produced (maximum values of MW content of around 26 g kg^{-1}), even the water parcels with the highest MW concentrations will appear warmer, more saline, and less oxygenated than WW because of the contribution from mCDW (Jenkins 1999). Within the water column across the continental shelf, MW will not be seen as a pure water type.

Previous studies have identified and quantified the MW directly in front of PIIS using temperature, salinity, and dissolved oxygen concentrations (Jenkins 1999) and across the Amundsen Sea Embayment (Nakayama et al. 2013), as well as calculating annual melt rates and locating regions of increased outflow from the glacier (Thurnherr et al. 2014). The strongest outflow is observed on the southwestern side of the ice shelf, driven by geostrophy (Thurnherr et al. 2014). Across the front of the shelf the MW tends to lie above approximately 400 m depth, which correlates with the draft of the ice front (Jenkins et al. 2012). The melt rates deduced have been seen to vary between different years (Dutrieux et al. 2014), with the highest melt rates in 2009 and 2010 and a recent decrease in 2012. This variability in calculated melt rate has been attributed to changes in the strength of the circulation under the ice shelf (Jacobs et al. 2011) and changes in the amount of heat transported onto the continental shelf, possibly linked to local or regional winds (Dutrieux et al. 2014; Jenkins et al. 2016).

The mCDW flows onto the eastern Amundsen Sea continental shelf through bathymetric channels situated

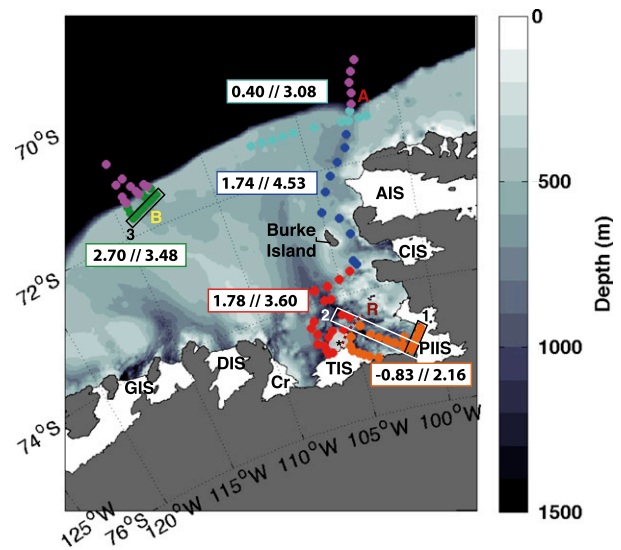


FIG. 1. Map showing the CTD stations from iSTAR, split into characteristic regions: purple = off shelf, cyan = shelf edge (east), blue = eastern channel, green = shelf edge (central), red = outer PIB and Thwaites Ice Shelf (TIS), and Orange = inner PIB and PIIS. The black or white rectangular boxes (also numbered) relate to different sections plotted in Figs. 4–7, and the letters A and B show the two main channels into the eastern Amundsen Sea: A = eastern channel, B = central channel. Burke Island is labeled as well as the ridge (R) separating the PIB and PIIS CTD groupings. The asterisk marks an area of fast ice in front of TIS. Local ice shelves are also labeled: Abbot Ice Shelf (AIS), Cosgrove Ice Shelf (CIS), Crosson Ice Shelf (Cr), Dotson Ice Shelf (DIS), and Getz Ice Shelf (GIS). The numbers in the colored rectangular boxes relate to the area created by curvature in the CDW–WW mixing line, with the first number relating to Θ – S_A space and the second number relating to $c(\text{O}_2)$ – S_A space.

at 103° W (eastern channel) and 114° W (central channel; Fig. 1). Off shelf the CDW consists of Upper CDW (UCDW; temperature greater than 1.5° C, practical salinity greater than 34.50, and the oxygen minimum) and Lower CDW (LCDW; practical salinity greater than 34.70, temperature cooler than UCDW) components (Orsi et al. 1995). The mCDW that is present on the continental shelf is some mixture of these two components, with the warmest waters observed in the eastern channel (up to 1.25° C, 34.88 g kg^{-1}), and cooler waters (1.2° C, 34.87 g kg^{-1}) in the central channel, using the Thermodynamic Equation of Seawater 2010 (TEOS-10) for conservative temperature and absolute salinity (Nakayama et al. 2013; IOC et al. 2010). Variability in these regions of on-shelf flow has been observed through moorings (Assmann et al. 2013) and simulated in modeling of the region (Thoma et al. 2008): the variability is most often reflected as changes in the thickness of the mCDW layer on the continental shelf (Wählin et al. 2013).

The mCDW melts PIIS from below, and the strongest potential for melting is at the grounding line (where the

higher pressure results in a reduced melting point of ice). However, a ridge crosses the PIIS cavity (Jenkins et al. 2010), reducing the water depth to 200–300 m (between the base of the ice shelf at around 400 m and the top of the ridge at approximately 600–700 m). This means that the thickness of mCDW will have a direct impact on the temperature of the water that has access to the inner cavity of PIIS and consequently will affect circulation and melt rates (Jacobs et al. 2011).

Kim et al. (2016) have used noble gas measurements to identify MW from Dotson Ice Shelf at the edge of the continental shelf, approximately 300 km away from the ice shelf. However, noble gas analyses are expensive and laborious. For these reasons it would be beneficial to calculate reliable MW fractions using standard hydrographic observations of profiles of temperature, salinity, and dissolved oxygen, even at greater distances (>250 km) from PIIS. Previously, MW from PIIS has been identified at the continental shelf edge in the Amundsen Sea, using standard hydrographic observations (Nakayama et al. 2013). However, it remains unknown to what extent these calculated meltwater fractions are affected by atmospheric interaction and mixing at the shelf edge.

Using observations from a research cruise in 2014 (Heywood et al. 2016), the water mass characteristics are discussed and MW content is calculated across the eastern Amundsen Sea (sections 2 and 3). The reliability of these observations is assessed with the use of a simple one-dimensional ocean model, with identification of subsurface processes that may result in false meltwater signatures (section 5). A modification to the MW identification method is suggested, revealing a MW pathway along the coast to the west (section 6).

2. Water masses in the Amundsen Sea

a. Hydrographic data

The Ice Sheet Stability Programme (iSTAR) cruise took place on the RRS *James Clark Ross* between January and March 2014, occupying 104 conductivity–temperature–depth (CTD) stations in total, shown in Fig. 1 (Heywood et al. 2016). Measurements were collected using a Sea-Bird Scientific SBE 911 tool with dual CTD sensors and an SBE 43 dissolved oxygen sensor. Temperature was calibrated using an SBE 35 deep thermometer (at depths where bottles were fired), and salinity was calibrated using a Guildline Autosol salinometer. Temperature and practical salinity were converted to conservative temperature Θ and absolute salinity S_A following TEOS-10 (IOC et al. 2010). Dissolved oxygen concentrations were calibrated using Winkler titrations.

b. Hydrographic observations

Three water masses on the continental shelf (mCDW, WW, and AASW) can be easily identified by their temperature, salinity, and dissolved oxygen concentrations (Figs. 2a, 3a). AASW occupies the top 50–100 m of the water column. The two components of CDW off shelf can be seen at the continental shelf edge (Figs. 2c–e, 3c–e). UCDW is the warmest portion of CDW (>1.5°C) and LCDW is a cooler, saltier, more oxygenated water mass below UCDW. These components are modified slightly from the Orsi et al. (1995) definitions of LCDW and UCDW, in part due to the distance from the southern boundary of the Antarctic Circumpolar Current (Orsi et al. 1995; Walker et al. 2013). Once on the continental shelf, the properties of the main three water masses vary spatially because of modification through mixing and atmospheric interaction (Nakayama et al. 2013).

By defining the mCDW endpoint as the warmest (and most saline) and the WW endpoint as the coolest below the surface layer in each CTD profile, variations in the characteristics of these water masses are seen across the continental shelf of the Amundsen Sea, similar to methods used by Nakayama et al. (2013). Using this endpoint identification, CTD stations were grouped into regions with similar properties (Table 1, Figs. 2, 3). These groupings will be used throughout this study and are shown by location in Fig. 1.

The warmest mCDW (1.3°–1.5°C) is found at the eastern shelf edge and along the channel to the east of Burke Island (Figs. 2d,f), with a cooler mCDW (1.21°C) in the central channel (Fig. 2e). The mCDW flows onto the continental shelf on the eastern side of the channels because of geostrophic steering (Schodlok et al. 2012; Nakayama et al. 2013). Further south, the densest mCDW ($\sigma_\theta = 27.81 \text{ kg m}^{-3}$), which was seen at the shelf edge, does not reach PIIS (black contour, Fig. 5). This means that the mCDW signature in front of PIIS originates from the slightly shallower waters that are cooler (1.13°C) and less saline (34.86 g kg^{-1} ; Fig. 2h). Dissolved oxygen concentrations [$c(\text{O}_2)$] at depth remain relatively constant ($187 \mu\text{mol kg}^{-1}$; Fig. 6). The mCDW directly in front of PIIS is cooler than has been observed in other years (Nakayama et al. 2013). This is likely due to a thinner mCDW layer than in the “warmer” years rather than actual temperature changes in the source CDW water off shelf (Nakayama et al. 2013).

The WW layer lies above the mCDW as a cooler, fresher, and more oxygenated water mass (Figs. 4–6). In the outer Pine Island Bay (PIB; as defined by Fig. 1) and closer to PIIS, the WW layer is warmer than elsewhere (–1.14°C), with higher salinity and lower oxygen concentration (as low as $256 \mu\text{mol kg}^{-1}$; Figs. 2g,h and Figs. 3g,h).

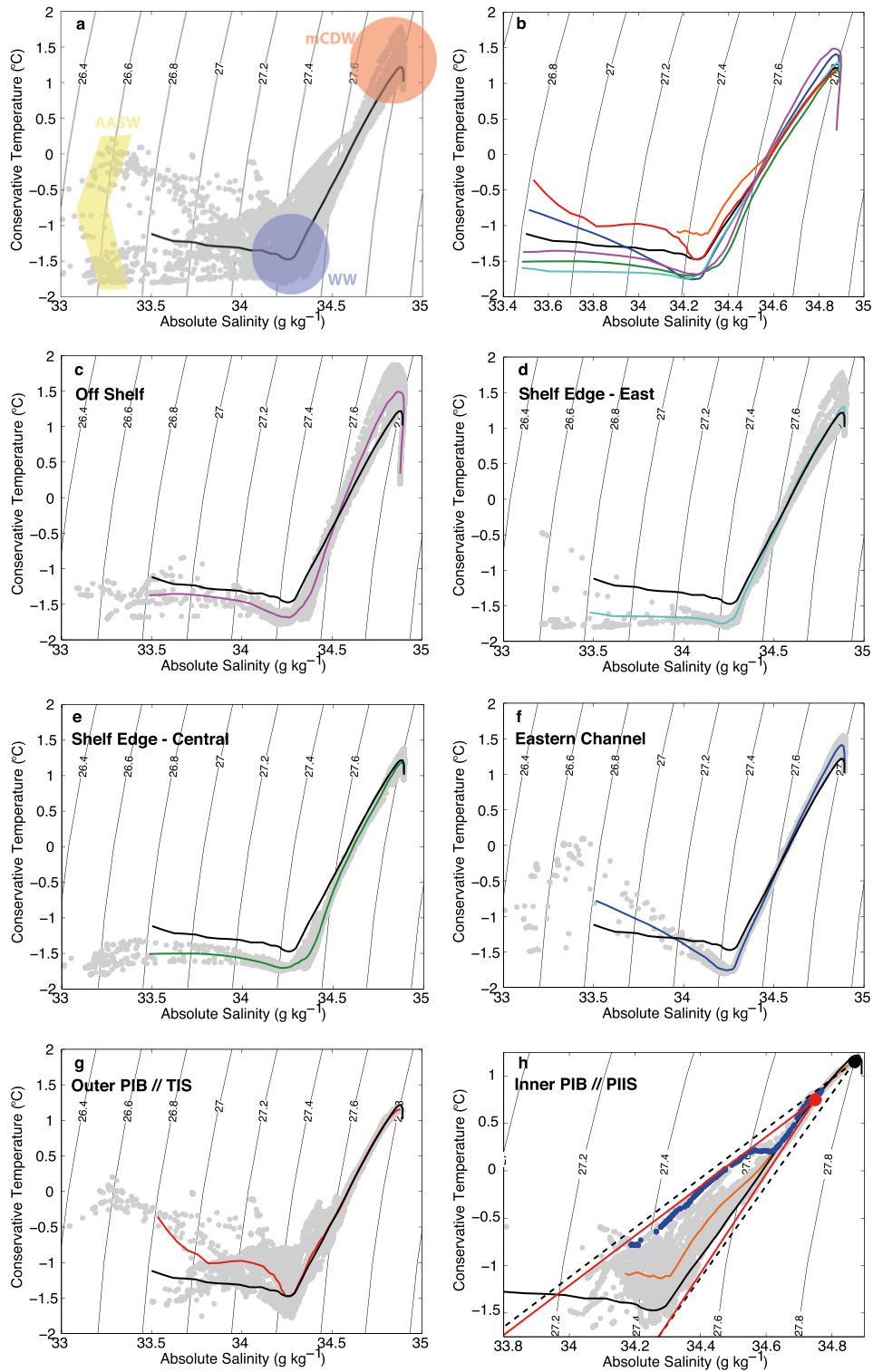


FIG. 2. Conservative temperature–absolute salinity (Θ – S_A) diagrams for the separate regions in the Amundsen Sea, using iSTAR data. On all panels, the density-average profile for all profiles is plotted in black. (a) All data plotted as gray dots. The main water masses (mCDW, WW, and AASW) are highlighted. (b) All of the mean profiles for each region, colored as in Fig. 1. (c)–(h) For each of the separate regions, the CTD data are plotted as gray dots, with the mean profile line plotted in color. Panel (h) also shows the mixing lines between mCDW–WW and mCDW–MW (black dot and black dashed lines) and the new pCDW–WW and pCDW–MW lines (red dot and red solid lines). The data collected from the strongest outflow of PIIS are shown in blue.

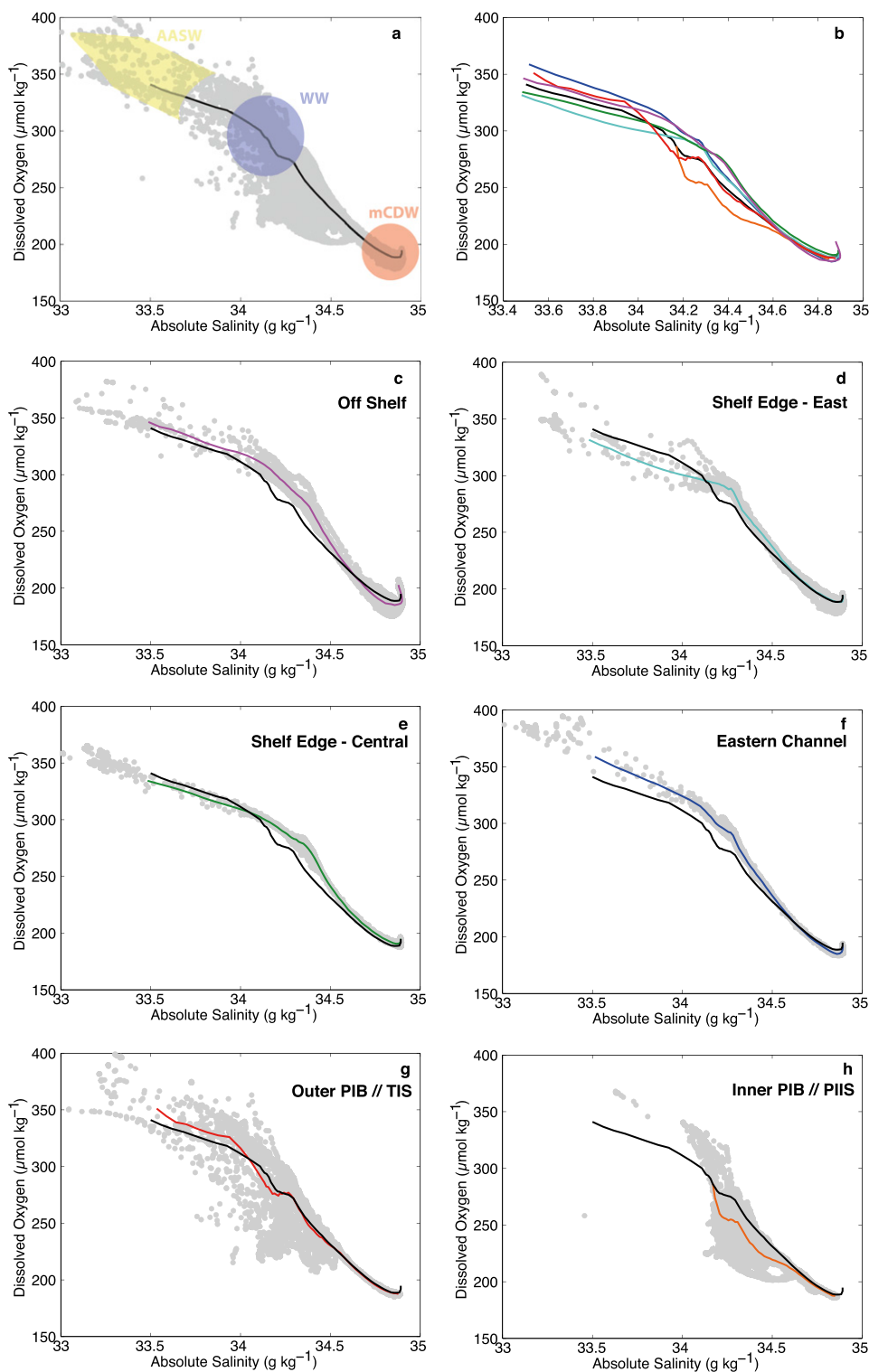


FIG. 3. Dissolved oxygen–absolute salinity [$c(\text{O}_2)$ – S_A] diagrams for the separate regions in the Amundsen Sea, using iSTAR data. (a) All data plotted as gray dots with the density-average profile plotted above in black. The main water masses (mCDW, WW, and AASW) are highlighted. (b) All of the mean profiles for each region, including the overall mean in black. (c)–(h) For each of the separate regions, all of the CTD data from that region are plotted behind the mean profile in gray dots, with the overall mean profile also plotted in black. The colored line represents the density-averaged values for that region, where the colors follow those shown in Fig. 1.

TABLE 1. Endpoints for mCDW and WW across the eastern Amundsen Sea, split into regions defined by the maximum mCDW temperature or the minimum temperature below the surface (WW). These regions relate to the different colored CTD stations in Fig. 1.

	Θ ($^{\circ}\text{C}$)	S_A (g kg^{-1})	$c(\text{O}_2)$ ($\mu\text{mol kg}^{-1}$)
mCDW			
Off shelf	>1.55	34.89	186
Shelf edge (east)	1.30	34.90	187
Shelf edge (central)	1.21	34.88	191
Eastern channel	1.41	34.88	186
PIB and TIS	1.15	34.87	187
PIIS	1.13	34.86	187
WW			
Off shelf	-1.67	34.28	288
Shelf edge (east)	-1.75	34.22	291
Shelf edge (central)	-1.68	34.34	282
Eastern channel	-1.76	34.27	291
PIB and TIS	-1.47	34.27	277
PIIS	-1.14	34.27	256

The increase in temperature and salinity and decrease in dissolved oxygen concentration compared with WW elsewhere in this region is likely associated with the MW that will be present in the area close to PIIS. The regions that are close to the coast (e.g., eastern channel and both PIB regions) have more saline and colder WW endpoints than elsewhere in the study area (Figs. 2f–h compared with Figs. 2c–e). This could be due to sea ice distribution: these regions may see more sea ice production than sea ice melt, similar to Stammerjohn et al. (2015).

3. Glacial meltwater calculations

a. Optimum multiparameter analysis

To identify MW, the characteristic properties (typically temperature, salinity, and dissolved oxygen concentration) of each water mass in the region must be known. Together, these properties are known as the water mass endpoint. Once these characteristics are known, two methods have typically been used around Antarctica to calculate MW concentration: a composite tracer method (Jenkins 1999) and optimum multiparameter analysis (OMPA; Tomczak 1981; Loose and Jenkins 2014). Both of these calculation methods rely on a set of simultaneous equations to produce the fraction of each water mass. The main difference between the two methods is that while the composite tracer method is an exact system (same number of tracers as unknowns, when mass conservation is included as a tracer), OMPA is an overdetermined system (where there are more tracers than unknowns, when mass conservation is included as a tracer). Where these water

mass calculations agree, the results (water mass fractions) will be the same. It is when they disagree that the methods employ different strategies to get to the results.

The overdetermined system used in OMPA results in a larger water mass fractions matrix (\mathbf{A} , where $A_{1,k}$ signifies the value of tracer 1 for water mass k) and observations array (\mathbf{b} , where b_1 signifies the observational value of tracer 1) than the water mass fractions array (\mathbf{x} , where k , l , and m are the three water masses):

$$\begin{pmatrix} A_{1,k} & A_{1,l} & A_{1,m} \\ A_{2,k} & A_{2,l} & A_{2,m} \\ A_{3,k} & A_{3,l} & A_{3,m} \\ 1 & 1 & 1 \end{pmatrix} \begin{pmatrix} x_k \\ x_l \\ x_m \end{pmatrix} = \begin{pmatrix} b_1 \\ b_2 \\ b_3 \\ 1 \end{pmatrix}, \quad \text{and} \quad (1)$$

$$\mathbf{Ax} = \mathbf{b}. \quad (2)$$

For this study, we use OMPA to calculate the glacial meltwater fractions because of the ability to use all available tracers and to weight each tracer depending on uncertainties that may be associated with that tracer. AASW is excluded from this analysis because of the wide range of possible endpoints (in the tracers used here), and so OMPA is only applied below 75 m. OMPA is well described in previous papers (Tomczak and Large 1989; Beaird et al. 2015; Loose and Jenkins 2014). In OMPA, the water mass fractions are calculated by minimizing the weighted sum of the squares of the residuals (\mathcal{D}^2) between the real ocean observations of the tracers and simulated tracer values calculated using the “best estimate” of the water mass fractions:

$$\mathcal{D}^2 = (\mathbf{Ax} - \mathbf{b})^T \mathbf{W}^T \mathbf{W} (\mathbf{Ax} - \mathbf{b}), \quad (3)$$

where \mathbf{W} is the weighting matrix and \mathbf{W}^T signifies the transpose of the matrix \mathbf{W} .

A nonnegativity constraint is also applied, as the water mass fractions must be positive. To balance the various tracers used, the tracers are normalized, using the standard deviation and mean values of each tracer (matrix \mathbf{A} becomes G , and \mathbf{b} becomes d). The tracers are also weighted to account for differing reliabilities. The weighting of the tracers (W_{ii}) is described as

$$W_{ii} = \frac{\sigma_i^2}{v_i}, \quad \text{and} \quad (4)$$

$$\widetilde{G}_{ij} = G_{ij} W_{ii} \quad \text{and} \quad \widetilde{d}_i = d_i W_{ii}, \quad (5)$$

where σ_i^2 is the variance associated with the endpoint i , v_i is the uncertainty associated with the tracer i (where the uncertainty consists of both analytical and environmental uncertainties), \widetilde{G}_{ij} is the weighted (and normalized) water mass characteristics matrix, and \widetilde{d}_i is the weighted (and normalized) observational data array.

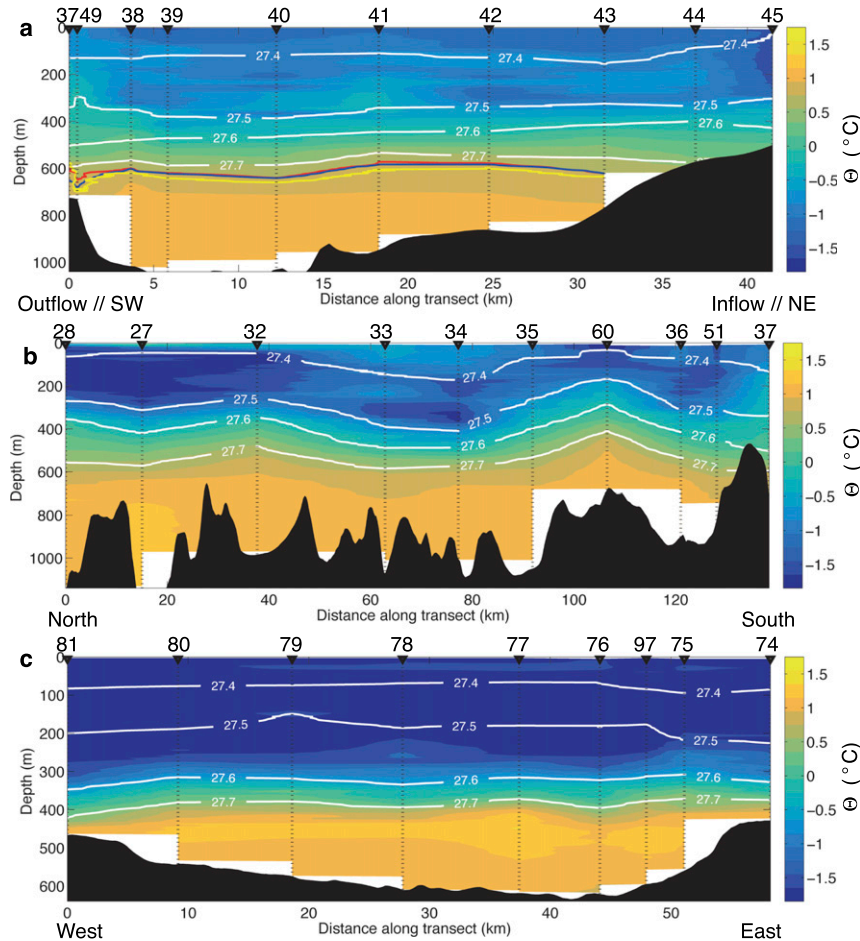


FIG. 4. Hydrographic sections of conservative temperature for (a) section 1 across PIIS, (b) section 2 traveling away from PIIS, and (c) section 3 across the central channel. Isopycnals of potential density are shown in white, and the locations of the CTD stations are shown as black triangles. Panel (a) also shows the contours for $\Theta = 0.76^{\circ}\text{C}$ (red), $S_A = 34.75 \text{ g kg}^{-1}$ (blue), and $c(\text{O}_2) = 194 \mu\text{mol kg}^{-1}$ (yellow).

The composite tracer method as described by Jenkins (1999) is useful for the obvious graphical interpretation of what the calculation is doing: the appearance of MW can be identified on a property–property diagram of two of the tracers as an excursion from the ambient mixing line between mCDW and WW (Fig. 2h). The ambient mixing lines for mCDW–WW and mCDW–MW can be plotted onto any property–property diagram (black dashed lines in Fig. 2h), allowing visual identification of the presence of meltwater. Appropriate water mass endpoints must be selected for the dataset under consideration.

b. Water mass endpoints

A vital component of water mass identification is the water mass endpoint matrix **A**. To construct this matrix, the characteristic tracer properties (or endpoints) for

each water mass must be known. This study chooses the mCDW endpoint from values in PIB (Fig. 1) and the WW endpoint from the eastern channel (Table 2), a similar methodology to Nakayama et al. (2013). The mCDW in PIB is representative of the water that will be traveling underneath the ice shelf and has values of $\Theta = 1.15^{\circ}\text{C}$, $S_A = 34.87 \text{ g kg}^{-1}$, $c(\text{O}_2) = 187 \mu\text{mol kg}^{-1}$ (Table 2). However, the WW in this region is modified by MW addition, and so WW values from the eastern channel of $\Theta = -1.76^{\circ}\text{C}$, $S_A = 34.27 \text{ g kg}^{-1}$, $c(\text{O}_2) = 291 \mu\text{mol kg}^{-1}$ are used instead (Table 2). The MW endpoint is assumed to be unchanging, but with a large uncertainty. The uncertainty is due to the fact that pure MW cannot be directly analyzed and so must be derived from far-field observations, theoretical calculations, or the gradient of the mCDW–MW mixing line observed in the strongest outflow of the glacier (Jenkins et al. 2010;

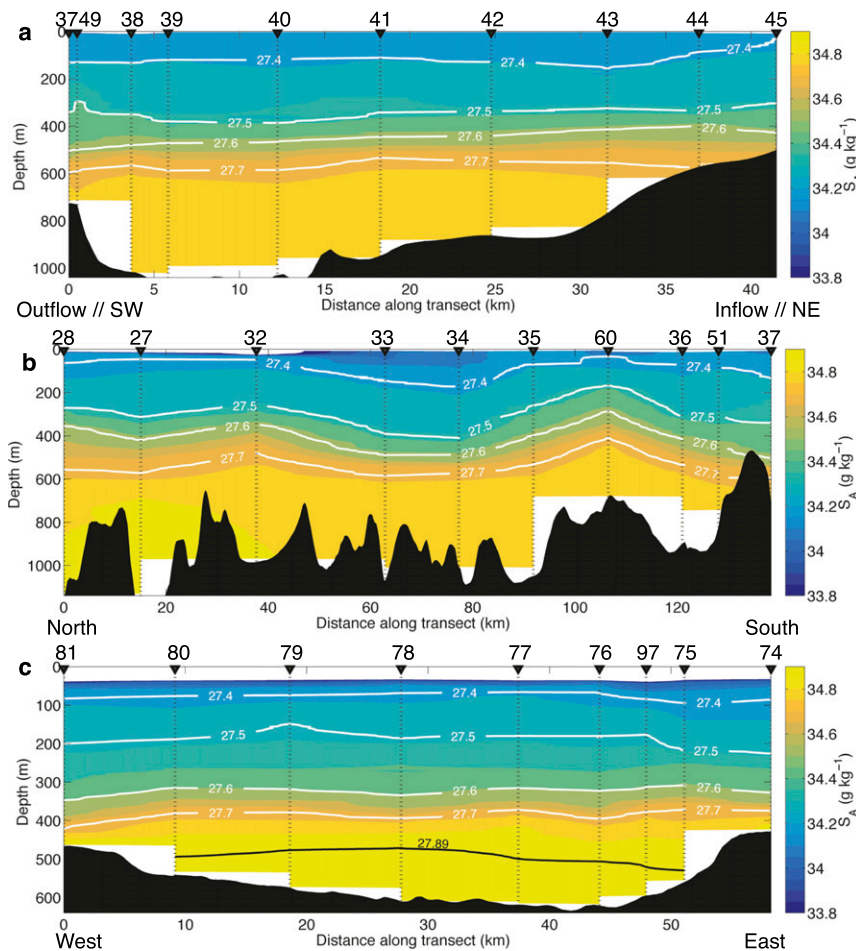


FIG. 5. As in Fig. 4, but for absolute salinity. The black line in (c) shows $\sigma_{\theta} = 27.89$, the limit for the warmer mCDW.

Jacobs et al. 2011). The MW endpoint that is used in this study comes from a combination of all three of these methods: $\Theta = -90.8^{\circ}\text{C}$, $S_A = 0\text{ g kg}^{-1}$, and $c(\text{O}_2) = 1125\ \mu\text{mol kg}^{-1}$. The Θ value for MW is a purely theoretical value that accounts for the freezing enthalpy. This study uses the same value as Nakayama et al. (2013).

The uncertainties associated with these endpoints are used in OMPA in order to weight the tracers. The uncertainty (and consequential weighting) for each tracer is shown in Table 2. As the MW is not directly analyzed it carries the largest uncertainties, so these uncertainties are used for the weighting of the tracers in OMPA.

c. Glacial meltwater fractions in 2014

The MW fractions calculated using endpoints defined in section 2b are reported as g kg^{-1} and are shown in sections across the front of PIIS, perpendicular to PIIS, and across the central trough (sections highlighted in Fig. 1, MW content shown in Fig. 7). As distance from

the front of the ice shelf increases, the MW fraction generally decreases.

The distribution of MW in front of PIIS (Fig. 7a) is similar to previous years (Jacobs et al. 2011; Nakayama et al. 2013), with the highest concentrations on the southern edge of PIIS (where the outflow is observed) and the lowest concentrations on the northern edge. It occurs at depths of 500 m or shallower, which is due to the depth of PIIS (Jenkins et al. 2010). Further from PIIS along the meridional section (Fig. 7b), the meltwater appears in patches along the $27.5\text{--}27.7\text{ kg m}^{-3}$ isopycnals.

To identify meltwater pathways, the meltwater calculation needs to be reliable at the continental shelf edge of the Amundsen Sea. Across all of the sections (Fig. 7), there is an apparent meltwater intrusion between the 27.5 and 27.7 kg m^{-3} isopycnals, which occurs at approximately 400 m depth. This intrusion can be identified all the way out to the shelf edge and, if

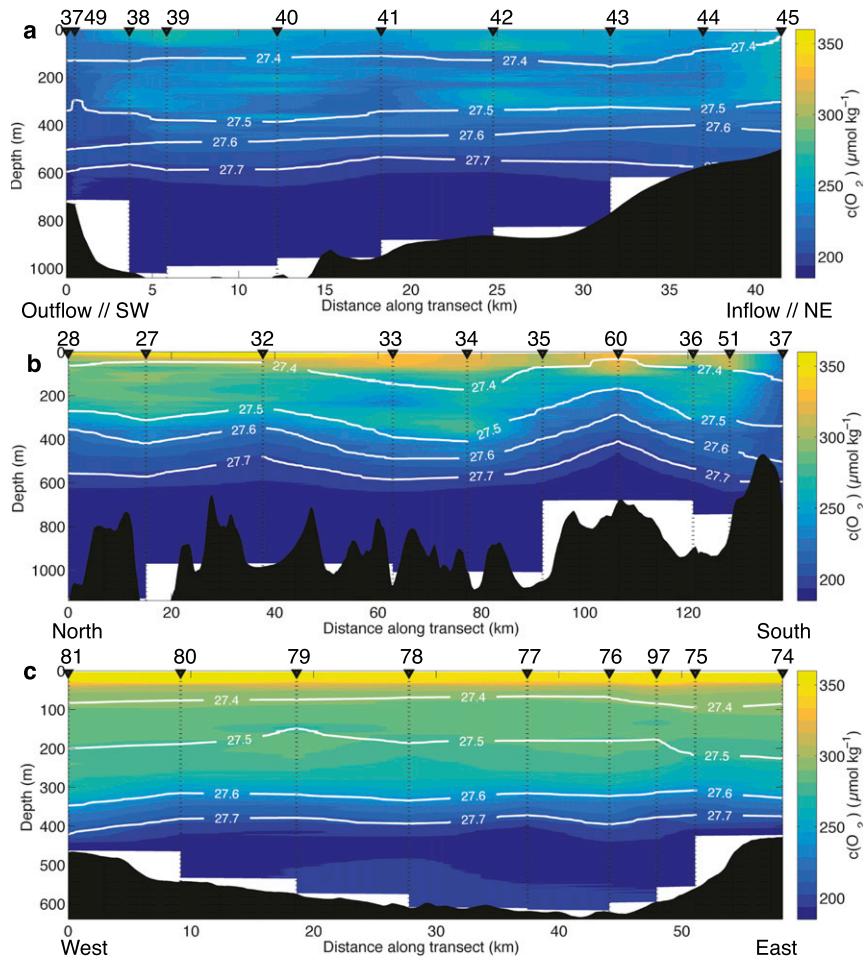


FIG. 6. As in Fig. 4, but for dissolved oxygen concentrations.

reliable, could signify a clear route that the meltwater takes after it leaves the ice shelf.

In both the Θ - S_A and $c(O_2)$ - S_A diagrams (Figs. 2, 3), a curvature in the mCDW-WW mixing line can be seen, especially in the $c(O_2)$ - S_A diagram. This indicates a position of the water properties off the ambient mixing line in the mCDW-MW-WW mixing space, which will result in the meltwater signature observed. At the isopycnals where the meltwater intrusion is located, the profile curves away from the ambient mixing line—significantly so in $c(O_2)$ - S_A space. Yet what is notable about this curvature is that it occurs in all of the profiles in $c(O_2)$ - S_A space (Fig. 3) and a large number of the profiles in Θ - S_A space (Fig. 2). This homogeneity of curvature across all CTD stations suggests that whatever causes this curvature is widespread across the Amundsen Sea. Modeling of the ocean circulation on the shelf indicates that the MW outflow is expected to flow westward and along the coast after leaving PIIS, so this curvature may not be entirely caused by

meltwater (Nakayama et al. 2014). To determine whether this is reliably meltwater or not, we must consider alternative processes that may result in a false meltwater signature.

4. Curvature in property-property profiles

To say whether the curvature that is observed in the property-property diagrams is reliably meltwater or not, we must consider alternative processes that may result in a false meltwater signature. If the entire curvature is not due to meltwater, then it can be assumed that this other process contributes up to 4 g kg^{-1} uncertainty into the meltwater fraction calculations, as this is the maximum MW fraction observed in the shelf edge section at approximately 400 m depth (Fig. 7). To understand what process could be providing an excess of heat for a given salinity (and loss of dissolved oxygen concentrations) to cause this curvature, the curvature must be quantified.

TABLE 2. Endpoints used throughout this study for mCDW, WW, MW, and pCDW. Uncertainties ν estimated from spread in endpoints on property plots, or errors associated with MW endpoints and used to calculate the weightings W .

	mCDW	WW	MW	pCDW	ν	W
Θ ($^{\circ}\text{C}$)	1.15	-1.76	-90.8	0.76	1.2	2277
S_A (g kg^{-1})	34.87	34.27	0	34.75	0.1	3984
$c(\text{O}_2)$ ($\mu\text{mol kg}^{-1}$)	187	291	1125	194	400	661

a. Quantifying the curvature

To quantify the curvature, it is important to first normalize the different tracers, as each tracer has different ranges in possible values. This range in values for the tracers could cause the curvature to appear greater in $c(\text{O}_2)$ - S_A space than Θ - S_A space, as $c(\text{O}_2)$ has a larger range than Θ . Therefore, the properties are normalized to a range between 0 and 1. The area between the linear mixing line (mCDW-WW) for each region and the curve formed by the data is used as a parameter to assess the curvature (Fig. 8e). The magnitude of this area changes between the different regions and different properties (values are annotated on Fig. 1).

The curvature in Θ - S_A space is negligible at the eastern continental shelf edge and directly in front of PIIS and is relatively small in the eastern channel and in PIB ($<1.8 \times 10^{-3}$; Fig. 1). However, at the central shelf edge, this curvature becomes more noticeable, and the area under the curve here reaches 2.7×10^{-3} . In comparison, the curvature in $c(\text{O}_2)$ - S_A space is apparent in all regions of the Amundsen Sea and is relatively homogeneous (approximately 3.5×10^{-3} ; Fig. 1). It is greatest in the eastern channel (4.53×10^{-3}).

Even if some of the curvature is caused by meltwater, the spatial variability suggests that there is at least one, possibly two, additional processes affecting the curvature. The first process affects all three properties and is greatest at the central shelf edge, with minimal effect in front of the ice shelf. The second process only appears to affect $c(\text{O}_2)$ and is relatively homogeneous across the continental shelf. These two processes could also produce the curvature without any input from meltwater, so alternative hypotheses are important to consider in order to understand what causes this curvature and its effect on the meltwater calculation.

The curvature tends toward lower $c(\text{O}_2)$, lower S_A , and higher Θ , so any processes to be considered must in some way simulate these changes. All subsurface water mass transformations must be linked to physical or biological processes. Working from this foundation, two general processes can be identified that could affect water mass properties: water mass addition and biological respiration.

b. Water mass addition

In the Amundsen Sea region there is no deep water formation, limiting the water masses on shelf to the four previously discussed: AASW, WW, mCDW, and MW. The MW addition has already been considered as a subsurface process in the Amundsen Sea, but it may not account for the curvature observed in the data between mCDW and WW endpoints because of the spatial variability seen between the curvature in Θ - S_A and $c(\text{O}_2)$ - S_A space. So if another water mass has been added to the subsurface water column, what are its possible sources?

The WW forms annually through heat loss to the atmosphere and so is affected by the meteorological conditions each year: this interannual variability could cause variability in the endpoint. In colder winters, more sea ice will be produced, resulting in a more saline, slightly colder (due to the lowering of the freezing temperature) and less oxygenated (due to sea ice cover) WW being formed. This colder WW endpoint will create a new mixing line, connecting with the previous ambient mCDW-WW mixing line at some depth (Figs. 8a,b), resulting in a curvature of the apparent mixing line.

MCDW derives from off-shelf CDW, which consists of UCDW and LCDW. There is no observational evidence for the presence of warm UCDW on the continental shelf, and the warmest waters on shelf likely reflect an LCDW endpoint instead (Fig. 2). The switch between UCDW and LCDW off shelf to just an LCDW component on shelf could result in the upper water column retaining a mixing line between WW and UCDW (from off-shelf properties), but the lower water column would mix between some point along the WW-UCDW mixing line and the LCDW component that moves on shelf. This produces a curvature of the apparent mCDW-WW mixing line, in the direction that is observed in the CTD data (Figs. 8c,d).

c. Biological productivity and respiration

Biological activity can affect dissolved oxygen concentrations through photosynthesis [increasing $c(\text{O}_2)$] and respiration [decreasing $c(\text{O}_2)$]. The curvature tends toward lower dissolved oxygen concentrations (Fig. 8f) and shows the greatest deviation at approximately 400 m depth (Fig. 7c), and so biological respiration is the most likely cause of depleted oxygen levels. The effect of respiration must be greatest at the depth of the greatest deviation from the mixing line (Fig. 8f). The deviation from the linear mixing line would therefore be greatest in regions of high respiration rates: this may explain why the curvature in $c(\text{O}_2)$ - S_A space is greatest in the eastern channel. This region showed visibly higher concentrations of chlorophyll *a* coloring the surface water green,

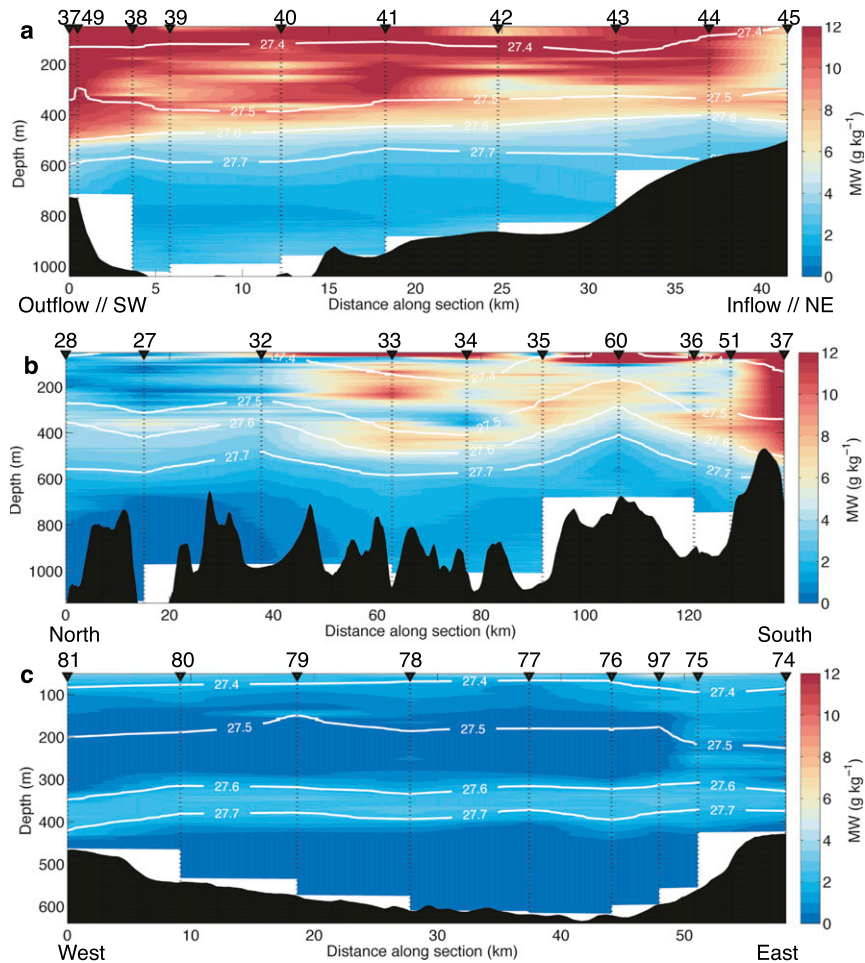


FIG. 7. As in Fig. 4, but for initial glacial meltwater content (MW_{MCDW}).

indicating the availability of organic matter, whose export would result in higher respiration at depth and potentially the curvature observed. Respiration rates were not measured during the cruise, and therefore a conceptual model was used to see how these processes may affect the water column.

5. One-dimensional ocean model in the Amundsen Sea

a. Description of the model

The model used in this study is the Price–Weller–Pinkel model (PWP; Price et al. 1986). PWP is a bulk mixed layer model, so it applies forcing over the entire mixed layer and averages the ocean properties over the mixed layer depth. For this study, the code from Lazarevich and Stoermer (2001) was used, which includes vertical diffusion (Lazarevich et al. 2004). The basic code is well described in that paper, but for this

study modifications were made to it (fully described in the appendix). These changes included the addition of a sea ice model, additional turbulent kinetic energy (TKE) parameterizations, and the inclusion of dissolved oxygen as a tracer. Both physical and biological processes were parameterized for the addition of dissolved oxygen into the model. The new model is referred to as the modified PWP (mPWP).

These additions allowed the model to simulate ocean processes in the Amundsen Sea, using ocean values (temperature, salinity, and dissolved oxygen concentrations) from CTD measurements to initiate the model and NCEP CFS climatology for air–sea fluxes to force the model (Saha et al. 2006).

b. Variations in the WW endpoint

Our hypothesis is that a year with lower air temperatures or stronger winds (resulting in greater latent heat flux to the atmosphere) than average will result in more sea ice production and so a more saline (and fractionally

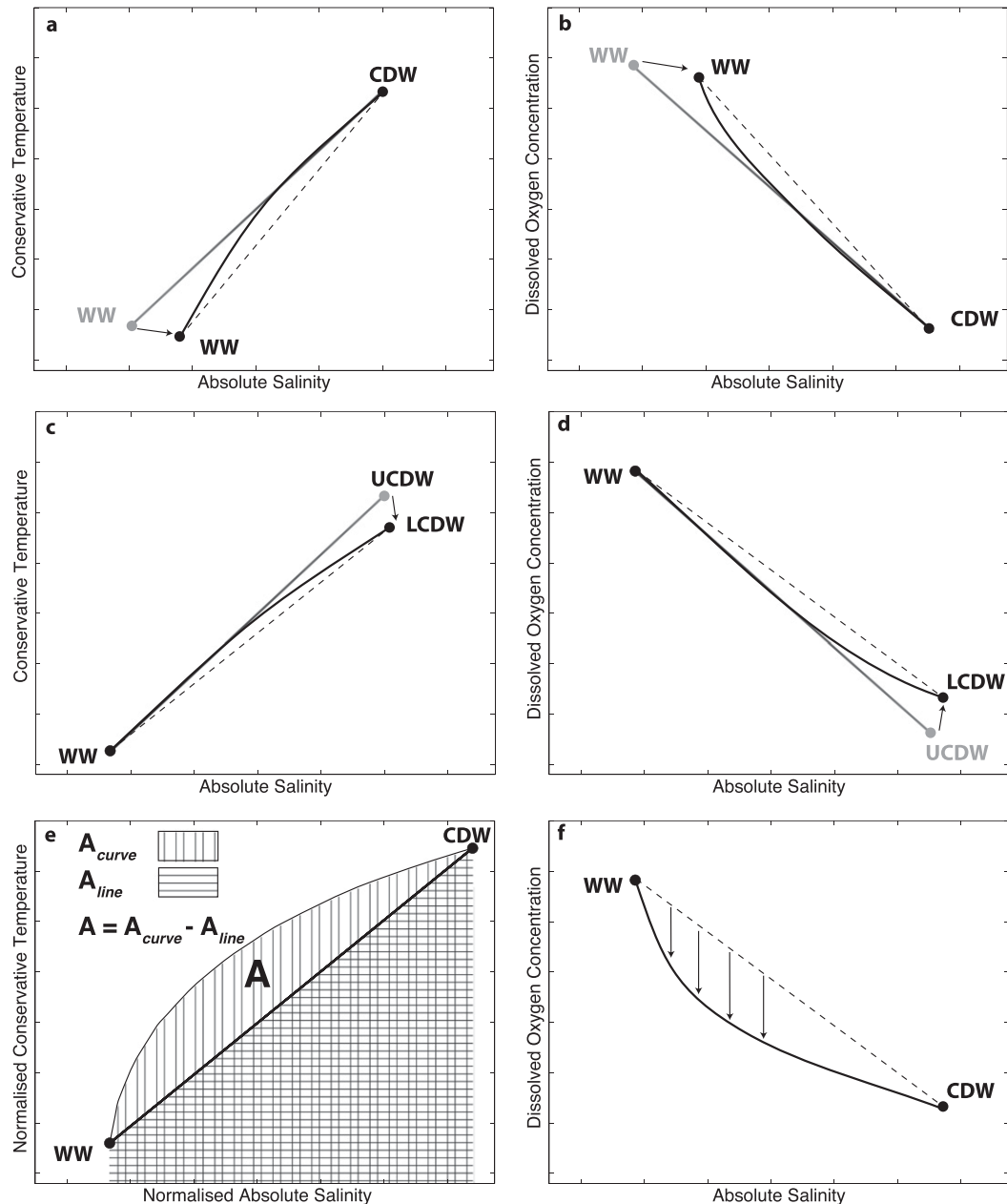


FIG. 8. Schematic diagrams showing how the curvature is quantified and the processes that might cause it. (a),(b) The curvature caused by a shift in the WW endpoint to more saline properties; (c),(d) the curvature caused by a switch between UCDW and LCDW endpoints for the source of the mCDW on shelf; (e) the curvature is calculated for each CTD grouping, where the curve is formed by the average CTD profile, and the linear line is formed using the localized CDW and WW endpoints; and (f) the curvature caused by biological respiration at depth, decreasing dissolved oxygen concentrations.

colder) WW endpoint. This shift in WW could result in curvature in the mixing line between mCDW and WW, causing an apparent increase in MW fraction in the OMPA calculations.

The model was run for 10 years, with the NCEP CFS climatology repeated each year. No biological processes

were included in order to separate the effects of the variation in WW and biological activity on the dissolved oxygen. As the one-dimensional model is unable to realistically advect sea ice out of the domain, the model grows more sea ice throughout the 10-yr run, resulting in a more saline and slightly colder WW endpoint

(WW'). This is the change in WW that we want to model, and so it is left in the model.

Over the 10-yr model run, in Θ - S_A space, the WW endpoint gradually shifts along the seawater freezing temperature line (gray lines; Fig. 9a) toward the colder and more saline values (final profile, red line; Fig. 9a). The final profile, after 10 years, shows clear curvature in the upper water column section of the mCDW-WW' mixing line, with the base of the water column still displaying the linear mCDW-WW mixing line. In $c(\text{O}_2)$ - S_A space, a curvature also forms over the 10-yr model run, with the WW' endpoint being more saline and more concentrated in dissolved oxygen (Fig. 9b). The dissolved oxygen concentration shifts to these much higher values because of the addition of oxygen through air-sea interaction. These dissolved oxygen concentrations would likely be reduced through biological respiration, which is not included at this stage of the model.

Overall, while this simulation of the production of the WW' endpoint shows curvature in the mixing line, the shape of curvature does not reflect what is observed in Θ - S_A or $c(\text{O}_2)$ - S_A profiles from the iSTAR data. The hydrographic observations show curvature at both ends of the mCDW-WW mixing line (Figs. 2e, 3e). In contrast, the profile produced by this simulation retains a linear mixing line at the base of the water column. This suggests that while variation in the WW endpoint can produce some curvature, it is unlikely to be the only process occurring at the central shelf edge.

c. Variations in the mCDW endpoint

The second hypothesis for what could be causing the curvature is variation in the mCDW endpoint. A switch from UCDW to LCDW at the shelf edge would result in a cooler, slightly more saline and more oxygenated endpoint. This is modeled in mPWP by running the model for 5 years with the UCDW endpoint, before switching the ocean column endpoint to the LCDW characteristics.

The switch between the endpoints can be seen clearly in the water mass characteristics (Figs. 9c,d). The curvature caused by the variation in the WW endpoint can still be seen at the WW end of the mixing line, but a midpoint from which both ends of the profile curve away is now visible (at a salinity of approximately 34.6 g kg^{-1}). This curvature replicates the shape seen in the hydrographic observations (Figs. 2e, 3e) much better, suggesting that both mCDW and WW variations modify Θ , S_A , and $c(\text{O}_2)$ at the central shelf edge.

d. Effects of biological activity

In addition to the curvature observed in Θ - S_A and $c(\text{O}_2)$ - S_A space at the central shelf edge, a more spatially

homogeneous curvature was seen in $c(\text{O}_2)$ - S_A (second values shown in Fig. 1). This was hypothesized (section 4c) to be due to a more regional process, such as biological respiration at depth. To test this, biological processes affecting the dissolved oxygen concentrations were introduced to the mPWP model, using a "varying WW" run with the UCDW endpoint fixed.

The profile produced (Fig. 9e) can be compared with the $c(\text{O}_2)$ - S_A diagram from the varying WW run (Fig. 9b). The most noticeable difference is that the mixing line now has lower dissolved oxygen concentrations than the initial mCDW-WW mixing line, and despite no change in the mCDW endpoint, there is a clear curvature throughout the entire profile. If the surface increase due to air-sea interaction is ignored, the portion of the profile with $S_A > 34.4 \text{ g kg}^{-1}$ replicates the shapes of the profiles seen in Fig. 3, indicating that biological respiration likely plays a role in causing the observed curvature in $c(\text{O}_2)$ - S_A space.

6. An alternative approach to MW calculations

a. Accounting for endpoint variation

To account for the possible variation in water mass endpoints, we reappraise the endpoint values used in the MW calculation (Table 2 and black lines in Fig. 2h). The mixing line between MW and the water mass that is melting the ice shelf (typically mCDW) can be identified from the CTD data collected in front of PIIS (CTD stations 37 and 49, blue profile; Fig. 2h). This location (at the southwestern end) is chosen as it is where the glacial meltwater has just emerged from under the ice shelf and so the meltwater signature is likely to be larger than the signature of any other processes (such as biological respiration) that could affect it (Jenkins and Jacobs 2008). However, this profile shows a different gradient to the previous mCDW-MW mixing line (black line; Fig. 2h), set by defining the mCDW, WW, and MW endpoints, and has a different intercept with the mCDW-WW mixing line (blue line; Fig. 2h). As this CTD profile is located in the strongest outflow from PIIS, the gradient of the line represents the true gradient of the mixing line between MW and the water mass melting the ice shelf (Jenkins 1999; Jenkins and Jacobs 2008). This new intercept is referred to as a pseudo-CDW endpoint (or pCDW). The pCDW endpoint will be specific to the observations collected each season: there is temporal variability in the properties of CDW that are transported onto the continental shelf, which is reflected in the characteristics of this pCDW endpoint.

The pCDW endpoint has values of $\Theta = 0.76^\circ\text{C}$, $S_A = 34.75 \text{ g kg}^{-1}$, and $c(\text{O}_2) = 194 \mu\text{mol kg}^{-1}$. The depth at

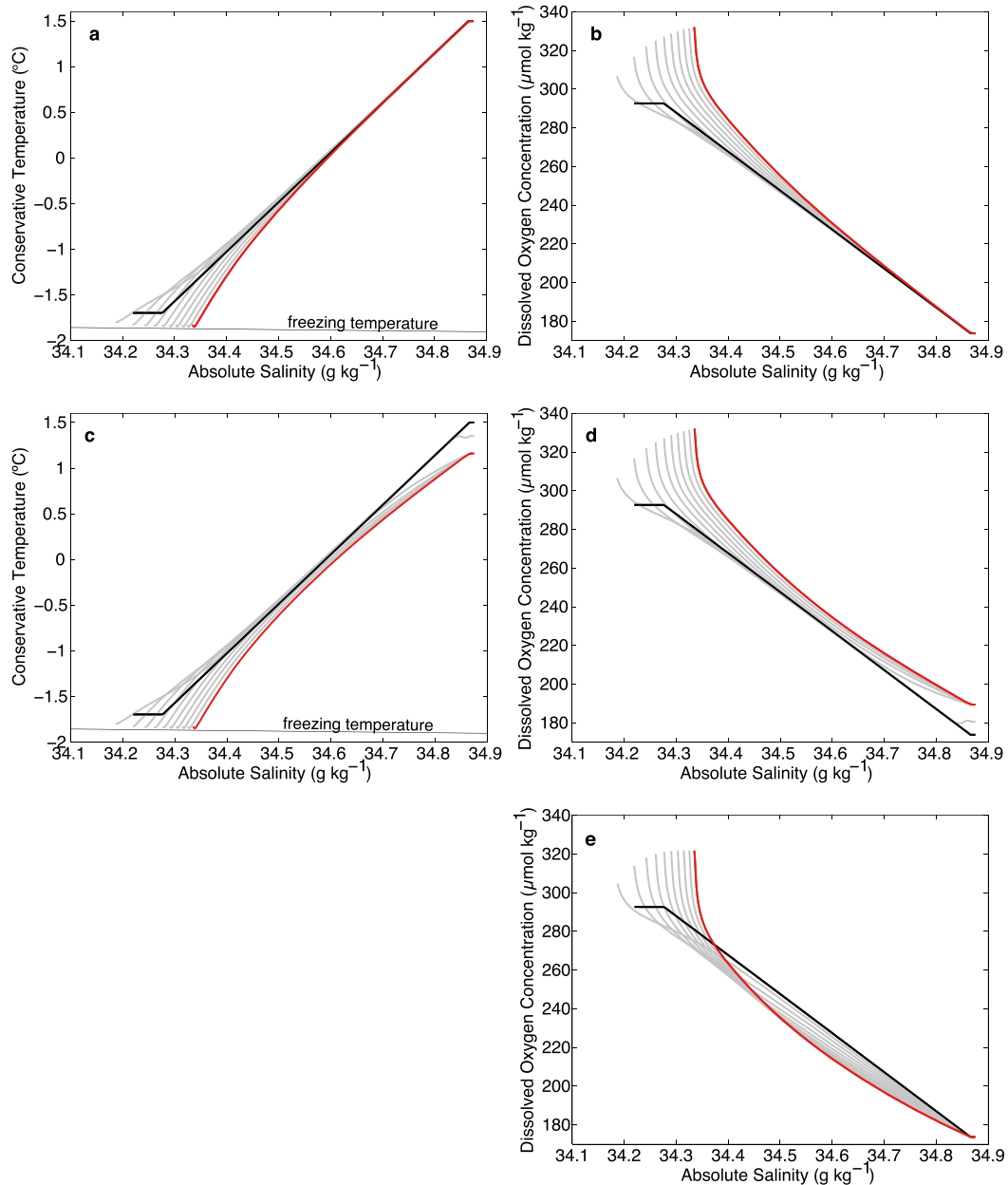


FIG. 9. (a),(c) Conservative temperature–absolute salinity and (b),(d),(e) dissolved oxygen–absolute salinity diagrams of a 10-yr mPWP model run with varying (a),(b) WW; (c),(d) mCDW; and (e) added NCP rates. The black line shows the initial profile (from 70 m depth to the base of the water column), with the gray lines showing the profile each year (years 2–9). The red line shows the final profile after 10 years. The mCDW endpoint is switched from UCDW (black line) to LCDW (end of red line) after 5 years run in (c) and (d). The temperature of the freezing point is also plotted in (a) and (c), showing the slight decrease in temperature with the increased salinity associated with sea ice production.

which these properties are found is shown by the contours [of Θ , S_A and $c(\text{O}_2)$] plotted onto the section of Θ across the front of PIIS (Fig. 4a). This shows that these pCDW properties occur at 600–700 m depth, consistent with the depth of the peak of the ridge beneath the ice shelf (Jenkins et al. 2010). This is significant, as the deepest

point of the water column that can theoretically reach the grounding line corresponds to the depth at which the water properties attributed to the pCDW endpoint can be found. Using this pCDW endpoint in water mass calculations that involve the identification of PIIS MW is appropriate; however, the S_A , Θ , and $c(\text{O}_2)$ values will be specific to

each season of observations and so will only identify recent glacial meltwater, rather than “older” or cumulative MW.

The model runs also show how increases in sea ice formation can cause changes in the WW endpoint and, consequently, curvature in the mCDW–WW mixing line. As the possible WW endpoints will range between less saline and more saline flavors, the best way to account for this in OMPA is to use the less saline WW endpoint, as this will provide the most conservative calculation. The use of this less saline WW endpoint is appropriate in the 2014 data from the Amundsen Sea, where the more saline WW endpoint is only observed at the central shelf edge.

b. Accounting for biological respiration

If the entire apparent increase in glacial meltwater fraction is assumed to be due to biological respiration, respiration has decreased the $c(\text{O}_2)$ values by approximately $15 \mu\text{mol kg}^{-1}$. However, the uncertainty in dissolved oxygen concentrations in the current OMPA is derived from the MW endpoint uncertainty ($200 \mu\text{mol kg}^{-1}$, section 2b). The $200 \mu\text{mol kg}^{-1}$ uncertainty from the MW endpoint is far larger than the uncertainty introduced by biological respiration ($15 \mu\text{mol kg}^{-1}$). This means that the glacial meltwater fractions are already heavily weighted toward Θ and S_A , and so no changes are made to the weightings in OMPA.

c. New glacial meltwater fractions in 2014

Using the new pCDW endpoint, glacial meltwater content was recalculated across the Amundsen Sea for PIIS MW from the 2014 iSTAR observations (MW_{PCDW} ; Fig. 10). Of particular interest are the changes in front of PIIS and at the central shelf edge. The original glacial meltwater (MW_{MCDW}) sections, the MW_{PCDW} sections, and the difference between the two calculation methods for these locations are shown for comparison (Figs. 7, 10, 11). At depths where $\sigma_\theta < 27.42 \text{ kg m}^{-3}$ and $\sigma_\theta > 27.73 \text{ kg m}^{-3}$, the MW_{PCDW} fractions are ignored (masked with lines or dots; Fig. 10), because these values are either associated with AASW or outside the mixing triangle (pCDW–WW–MW) when the new pCDW endpoint is used. This can be seen in the sections showing the difference between the calculation techniques: for depths where $\sigma_\theta > 27.73 \text{ kg m}^{-3}$ there is a negative residual, indicating higher values when the new pCDW endpoint is used (Fig. 11).

The apparent MW intrusion at the central shelf edge is now reduced to below 0.5 g kg^{-1} , which is within the noise signal (Fig. 10c), but there is still a coherent MW signature of approximately 4 g kg^{-1} between 200 and 400 m depth approximately 140 km from PIIS (Fig. 10b).

This supports the findings of Naveira Garabato et al. (2017), showing the MW settling along certain isopycnals found at these depths. The effect of using the pCDW endpoint can be seen clearly at the central shelf edge in Fig. 11c: the majority of the water column is unaffected, except for the specific layer that has been targeted with the changes to the OMPA calculation. While the model simulations showed that all three processes could cause the curvature that resulted in the apparent MW intrusion at the central shelf edge, the removal of this signature is most likely attributed to the change in the CDW endpoint from mCDW to pCDW. Since the use of the pCDW endpoint is specific to the characteristic endpoints of the iSTAR season, this signifies that if the curvature at the central shelf edge is due to glacial meltwater, it is either meltwater from a different source, or a different season, that is, from a source with different endpoints.

By integrating the MW fractions through the water column, we can obtain an estimate of the MW pathway. The apparent MW fractions are affected by solar radiation and sea ice melt at the surface and by the use of pCDW at depth, so the MW content is integrated between $\sigma_\theta = 27.42$ and 27.73 kg m^{-3} (Fig. 12a). Recent studies of the MW in front of PIIS shows that the MW will settle along isopycnals that are included within these limits, so by integrating over these density levels the main glacial meltwater signature is likely to be captured (Naveira Garabato et al. 2017). Because of the different mCDW endpoint used for the eastern channel, the CTD stations in this location are ignored because these stations show MW from the local ice shelves (Abbot Ice Shelf and Cosgrove Ice Shelf). The use of the lower bound of $\sigma_\theta = 27.42 \text{ kg m}^{-3}$ to remove the AASW results in the top 75–200 m being excluded. Some of this false surface MW fraction may be mixed down to below these depths, either through wind mixing events or convective mixing associated with sea ice formation. However, the percentage change in MW content from this relatively thin and stratified surface layer is minimal, and so this process is considered negligible. Oxygen isotopes could be used in the future to test this assumption. The use of this bound results in integration values in front of PIIS of as low as 1 m of glacial meltwater in 450 m of the water column, but a full water column integration results in values of 6–7 m of glacial meltwater in 600 m of the water column. This is due to the concentration of MW content at the surface in front of the strongest outflow from PIIS.

The water mass that is located between $\sigma_\theta = 27.42$ and 27.73 kg m^{-3} has a much higher MW content in front of PIIS and Thwaites Ice Shelf, and particularly

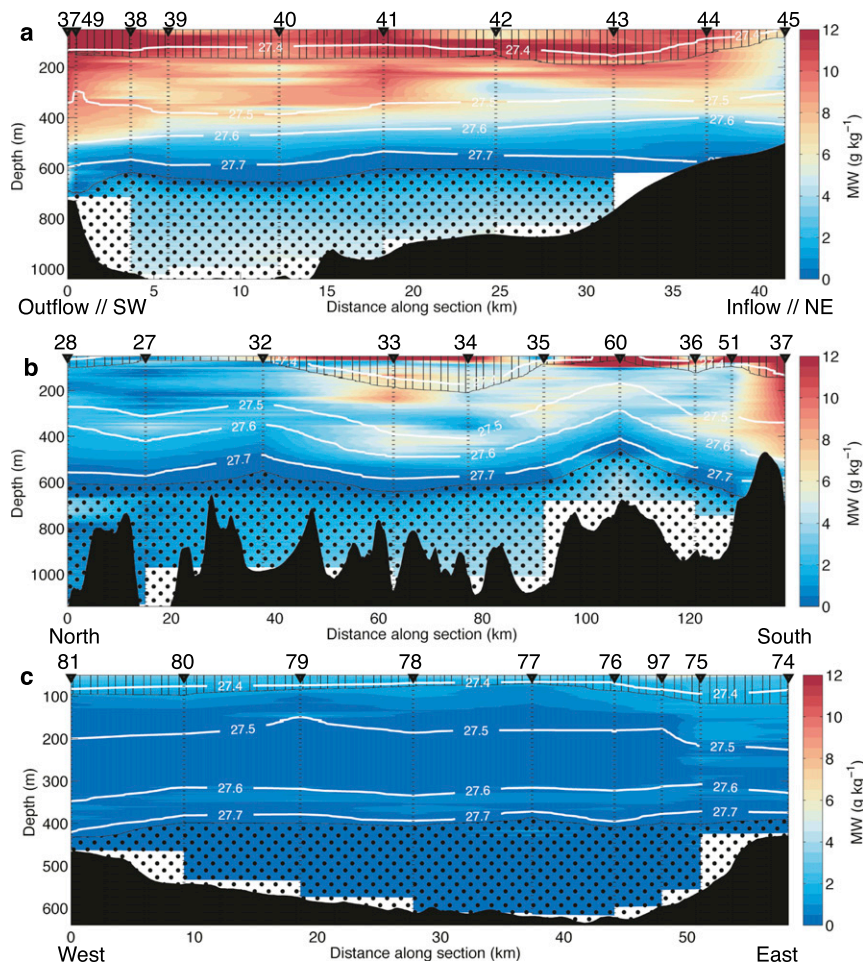


FIG. 10. Hydrographic sections of the new glacial meltwater content (MW_{PCDW}) for (a) section 1 across PIIS, (b) section 2 traveling away from PIIS, and (c) section 3 across the central channel. Isopycnals are shown in white, and the locations of the CTD stations are shown as black triangles. The depths where $\sigma_\theta < 27.42 \text{ kg m}^{-3}$ and $\sigma_\theta > 27.73 \text{ kg m}^{-3}$ are masked with lines or dots respectively.

toward the western side of the outer PIB, with values of up to 2.25 m of glacial meltwater in the water column (Fig. 12). The values at the central shelf edge are distinctly lower than those in front of PIIS, with a mean of 0.03 m of vertically integrated MW. Some of these stations in front of Thwaites Ice Shelf will include both PIIS and local Thwaites MW: the ratio of these inputs is an additional unknown. However, the combination of the coherent MW signature 140 km from PIIS and the low vertically integrated MW content at the central shelf edge indicate that the majority of the MW that leaves PIIS likely stays close to the coast. The MW observations shown by Nakayama et al. (2013) also suggest a westward flow along bathymetry, which the MW content calculated with the iSTAR data supports. By modifying the MW calculation to use the pCDW endpoint, and a slightly shifted WW endpoint, the MW

content is effectively removed at the central shelf edge, with several CTD stations reduced by 100% from their original MW fraction (Fig. 12b). In comparison, the percentage change in glacial meltwater content in front of PIIS is below 20%. This shows that the modifications to the calculation have a much larger impact at the shelf edge than in front of the ice shelf.

7. Discussion

The development of a one dimensional model revealed that the combination of varying WW properties and a switch between UCDW and LCDW endpoints for mCDW can replicate the curvature observed in Θ - S_A space. The most significant finding that emerged from inspecting the mCDW endpoint was that the “typical” mCDW endpoint should not necessarily be

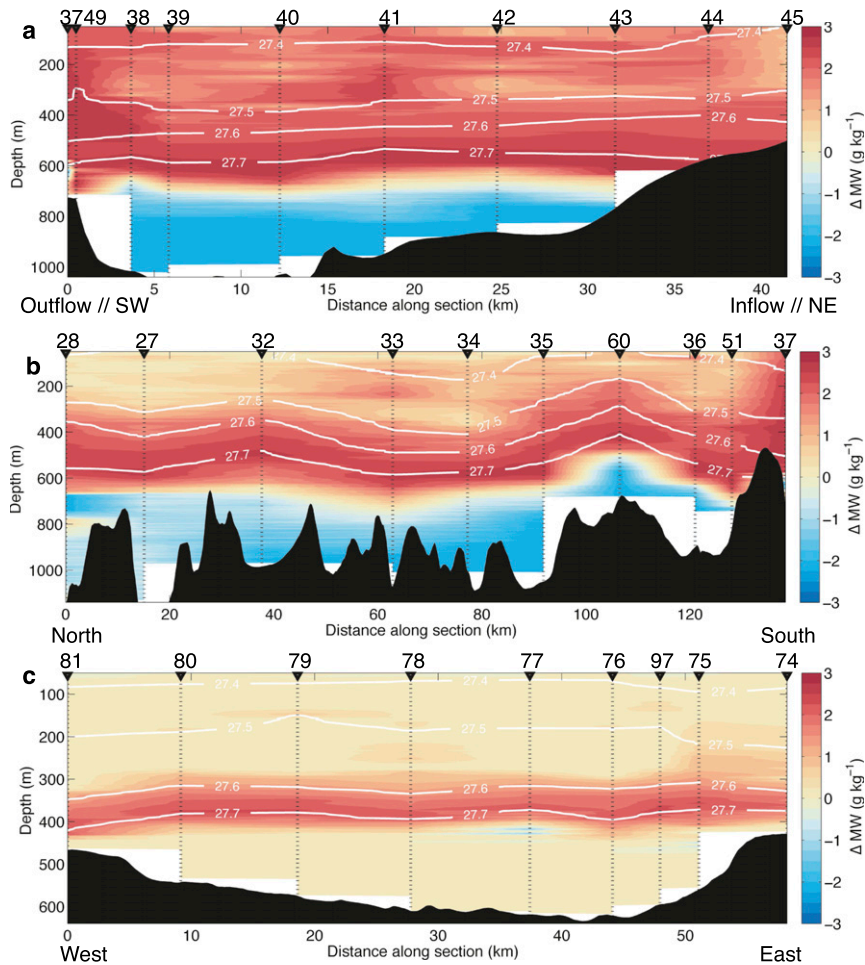


FIG. 11. As in Fig. 10, but showing the differences between the new and original glacial meltwater contents ($MW_{\text{MCDW}} - MW_{\text{PCDW}}$).

used. Typically, the mCDW endpoint is the temperature maximum found within PIB (approximately 1.16°C), but this does not necessarily equate with the waters that the glacial meltwater mixes with because of the ridge that stretches across the cavity underneath PIIS. Instead, properties from approximately 600–700 m depth should be used, creating a pseudo-mCDW endpoint (pCDW). This result highlights the importance of understanding the bathymetry underneath the ice shelf, as it can have a large impact on the ice–ocean interaction, and ice melt variability in the WW endpoint is likely to also affect the MW calculation, but investigation into these processes requires further work and would benefit from the use of oxygen isotopes to identify the volume of sea ice melt in the water column.

The alternative glacial meltwater calculations provide meltwater fractions for the 2014 iSTAR hydrographic dataset, showing glacial meltwater pathways from PIIS

(Fig. 12). Nakayama et al. (2014) modeled the spread of glacial meltwater from the Amundsen Sea, finding vertical integrations of glacial meltwater approximately 50% lower at the central shelf edge than the front of PIIS (2 m at the continental shelf edge and 4 m at PIIS). The vertically integrated glacial meltwater values calculated for the iSTAR data show a much bigger difference of approximately two orders of magnitude between the two locations (0.03 and 2.25 m). Whilst the meltwater values are similar between the model and observations in front of PIIS, the differences at the continental shelf edge could be due to different meteorological conditions (i.e., if we sampled a low meltwater year or the off-shelf transport was different due to variability in the winds), or the contribution of glacial meltwater from other sources or seasons (resulting in higher values in the model). It is encouraging for future development of computer models that the spatial distribution of PIIS meltwater (if not the exact values) is similar between the model and our observations.

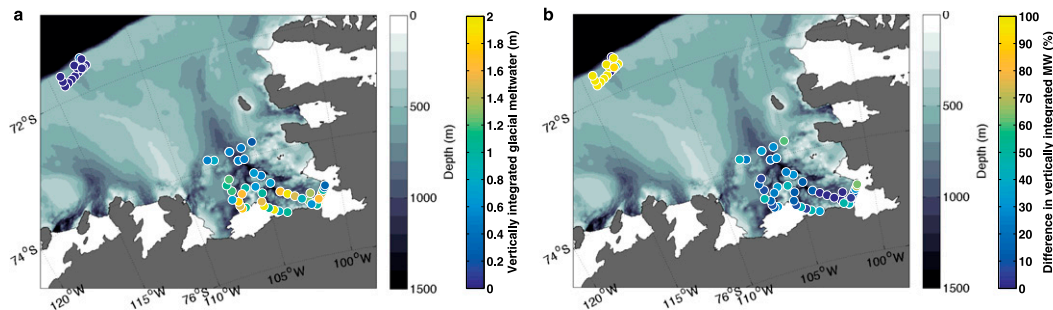


FIG. 12. Map of the Amundsen Sea showing CTD stations from in front of PIIS, PIB, and the central shelf edge (see Fig. 1). The bathymetry is shown in grayscale. Each CTD station is modeled by (a) the vertically integrated content of glacial meltwater (m) between $\sigma_\theta = 27.42$ and 27.73 kg m^{-3} and (b) the percentage difference ($MW_{\text{MCDW}} - MW_{\text{PCDW}}$) between the vertically integrated content of glacial meltwater.

The choice of pCDW endpoint is specific to the season that the observations were collected in, and this temporal variability is important to be considered. Our measurements and analysis have focused on data collected in 2014, but studies have identified the interannual variability that exists in this region (Jacobs et al. 2011; Dutrieux et al. 2014; Webber et al. 2017). This variability can affect the thickness of the mCDW layer, and therefore affects what properties exist at 600–700 m depth and can flow above the ridge. In some years with thicker mCDW layers, the values at 600–700 m depth may represent the warmest properties found on shelf, and so the pCDW method to remove curvature at the shelf edge will not be applicable. The use of the pCDW endpoint also restricts glacial meltwater identification to MW from PIIS that was produced in that season and may ignore “older” (or cumulative) glacial meltwater content.

This research has focused on the eastern portion of the Amundsen Sea and on glacial meltwater produced by PIIS, a warm-based ice shelf. There are many other glaciers terminating in the Amundsen Sea, including Thwaites Glacier—recently reported to be in irreversible retreat (Joughin et al. 2014)—and the Getz Ice Shelf, a significant contributor to rates of ice shelf volume loss in West Antarctica (Paolo et al. 2015). For these glaciers in the western Amundsen Sea, there will be additional glacial meltwater present from the glaciers and ice shelves farther to the east that has been transported in the coastal current. The glacial meltwater calculations in these regions will need to account for this additional background meltwater. In East Antarctica, recent studies have identified warm-based shelves (e.g., Totten Glacier) that show similar processes of ocean basal melting of the ice shelves in that region (Greenbaum et al. 2015). The ability to extrapolate the methods and findings made in this study to these locations around Antarctica would add significant knowledge of glacial meltwater pathways, which may help with future assessment of the effects

of glacial meltwater and potentially improve global ocean models.

8. Conclusions

This study has identified processes, or features, not discussed previously in the context of glacial meltwater calculations, highlighting the importance of understanding the effects of endpoint variability and biological activity on MW fraction calculations. By using an alternative calculation method, the glacial meltwater was seen to be concentrated to the western end of the ice shelf and close to the coast, similar to findings by Nakayama et al. (2013). These findings are shown schematically in Fig. 13.

Further data (such as noble gases and oxygen isotopes) will be beneficial to separate out the individual contributions from each of the processes implicated, which may result in more reliable meltwater pathways.

Acknowledgments. This work was supported by funding from the UK Natural Environment Research Council’s iSTAR Programme and NERC Grants NE/J005703/1 (L.C.B., K.J.H., J.K.) and NE/J005746/1 (A.J.). L.C.B. was supported by a PhD grant (1210192) from NERC and also thanks the feedback from Mark Brandon and David Stevens. All observational data are available from BODC, and L.C.B. can be contacted for model scripts.

APPENDIX

mPWP Model in the Amundsen Sea

a. Sea ice model

A simple thermodynamic sea ice model is introduced that uses the difference between the temperature of the surface of the ocean (T_1) and the freezing temperature

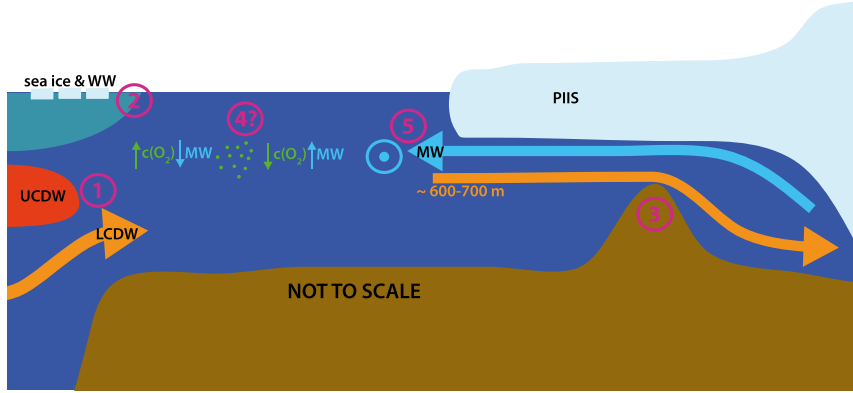


FIG. 13. Schematic showing the main conclusions from this study. Horizontal and vertical lengths are not to scale. 1) Influence of LCDW at the continental shelf edge is important to take into account. 2) Sea ice production/melt and WW variations may affect the upper water column. 3) The height of the ridge under the ice shelf blocks the deepest waters from accessing the grounding line (~600–700 m depth). 4) Biological productivity (respiration) increases (decreases) dissolved oxygen concentrations [$c(O_2)$], potentially affecting meltwater signatures. 5) Glacial meltwater emerges from under the ice shelf and is transported to the west (bullseye shows flow out of page).

(T_{fp} ; Fofonoff and Millard 1983) to calculate a melt rate (m) that is scaled by the mixed layer depth [Eq. (A1)]. The melt rate is used to calculate a sea ice thickness [h_i ; Eq. (A2)] as the product of melt, mixed layer thickness, and time (Δt). A sea ice fraction (A) is assigned one of two values depending on whether the sea ice is growing or melting [A_{grow} or A_{melt} ; Eq. (A3)]. These values are broadly representative of the values for sea ice concentration described by Stammerjohn et al. (2015). The assigned sea ice fraction is lower during periods of sea ice melt as a simple parameterization of advection of sea ice out of the model domain:

$$m = \frac{\rho_\theta}{\rho_{fw}} \frac{c_w}{L_f} (T_1 - T_{fp}) \frac{1}{\Delta t}, \quad (A1)$$

$$h_i(n+1) = h_i(n) - mh\Delta t, \quad \text{and} \quad (A2)$$

$$A_{grow} = 0.77, \quad A_{melt} = 0.6, \quad (A3)$$

where ρ_θ is the potential density, ρ_{fw} is the density of freshwater, c_w is the specific heat capacity of water, L_f is the latent heat of fusion and n is the time step. When sea ice is present, the mixed layer temperature is set to the freezing point and the mixed layer salinity is affected by the growth of the sea ice [Eqs. (A4), (A5)]. The sea ice salinity is set to zero for simplicity:

$$T_k = T_{fp}, \quad \text{and} \quad (A4)$$

$$S_k(n+1) = \frac{S_k(n)}{1 + (Am)}, \quad (A5)$$

for $(k-1)\Delta z < h$, where k is the mixed layer index.

On the next time step, the atmosphere–ocean heat and freshwater fluxes are reduced by the fraction of sea ice ($1 - A$), simulating a cover on the fraction of the ocean surface where sea ice is present [Eqs. (A6), (A7)]:

$$T_1(n+1) = T_1(n) + (1 - A) \frac{(Q_i \alpha_1 - Q_o) \Delta t}{\sigma_{\theta 1} c_w \Delta z}, \quad \text{and} \quad (A6)$$

$$S_1(n+1) = \frac{S_1(n)}{1 - (1 - A) Q_{fw} \left(\frac{\Delta t}{\Delta z} \right)}, \quad (A7)$$

b. Buoyancy and wind forced mixing parameterizations

Following Chen et al. (1994), the Kraus–Turner parameterization of TKE budgets was included in mPWP. These are used to calculate the vertical entrainment velocity at the base of the mixed layer that determines whether it shoals or deepens (Kraus and Turner 1967; Niiler 1975; Niiler and Kraus 1977). This requires recalculation of the new freshwater fluxes [after sea ice growth or melt is taken into account, F_{fw} ; Eq. (A8)],

$$F_{fw} = S_1 \left[(1 - A) Q_{fw} - Am \left(\frac{\Delta z}{\Delta t} \right) \right], \quad (A8)$$

as well as calculating the power supplied for mixing by wind stresses [P_w ; Eqs. (A9), (A10)]:

$$U_* = U \sqrt{\frac{\rho_a}{\rho_{fw}} C_d}, \quad \text{and} \quad (A9)$$

$$P_w = 2m_{kt}e^{-h/z_w}U_*^3, \quad (\text{A10})$$

where U_* is the friction velocity, U is the windspeed, ρ_a is the density of air, C_d is the drag coefficient, m_{kt} is the coefficient for power provided by wind, and z_w is the dissipation length scale. Buoyancy fluxes must also be calculated [P_b ; Eqs. (A11), (A12)]:

$$B = \left[\frac{g\alpha_T}{\rho_w c_w} (Q_o - 0.45Q_i) \right] - g\beta F_{fw}, \quad \text{and} \quad (\text{A11})$$

$$P_b = \frac{h}{2} [B(1 + n_{kt}) - |B|(1 - n_{kt})], \quad (\text{A12})$$

where B is the buoyancy term, α_T is the thermal expansion coefficient, β is the salinity contraction coefficient, and n_{kt} is the coefficient for power provided by buoyancy. The vertical entrainment w_e is then calculated as a balance between the power for mixing provided by the wind and buoyancy forcing, and the gravitational stability of the column [Eq. (A13)]:

$$w_e = \frac{P_w + P_b}{h[g\alpha_T(T_1 - T_k) - g\beta(S_1 - S_k)]}, \quad (\text{A13})$$

for $(k - 1)\Delta z = h + 1$. If the vertical entrainment is positive, the new mixed layer depth is adjusted by

$$\Delta h = w_e \Delta t, \quad (\text{A14})$$

and is recalculated until the increase in mixed layer depth is smaller than the grid cell. However, if the vertical entrainment is negative, then the new (shallower) mixed layer depth is calculated by balancing the wind mixing P_w with the buoyancy B :

$$h = \frac{P_w}{-B}. \quad (\text{A15})$$

This new mixed layer is then homogenized (as is required in a bulk mixed layer model) by mixing all of the properties within the layer.

c. Relaxation of the ocean column at depth

Without any replenishment of the mCDW at the base of the water column, the warm waters are gradually eroded by the cold WW' formed each season. To rectify this, a one-dimensional advection analog is introduced, which relaxes the ocean profile back to its original conditions (χ_{init}) below the depth at which CDW was generally observed during iSTAR (597 m). This follows the equation

$$\chi_k(n+1) = \chi_k(n) - V_{\text{adv}} [\chi_k(n) - \chi_k(1)] \frac{\Delta t}{\Delta x}. \quad (\text{A16})$$

The values used for Δx (10 km) and advective current speed (V_{adv} ; 0.01 m s^{-1}) in Eq. (A16) are based on approximate orders of magnitude from observations, but are also fitted to the model runs used in this study.

d. Addition of dissolved oxygen to the model

1) PHYSICAL PROCESSES

The exchange of oxygen between the atmosphere and the ocean is strongly influenced by wind speed, as greater wind speeds will result in greater turbulence and shear at the atmosphere–ocean boundary layer (Wanninkhof 2014). To model this process, the updated gas transfer velocity equation from Wanninkhof (2014) is used [Eq. (A18)]:

$$Sc = \nu/D, \quad \text{and} \quad (\text{A17})$$

$$k = 1.791 \times 10^{-5} U^2 (Sc)^{-0.5}, \quad (\text{A18})$$

where ν is the kinematic viscosity of the ocean surface, D is the molecular diffusivity of oxygen, Sc is the non-dimensional Schmidt number, and k is measured in meters per second. This velocity is then applied to the dissolved oxygen concentrations [$c(\text{O}_2)$] as

$$\Delta c(\text{O}_2) = - \left\{ k [c(\text{O}_2)_s - c(\text{O}_2)_{\text{sat}}] \frac{\Delta t}{h} \right\}, \quad (\text{A19})$$

where $c(\text{O}_2)_s$ is the surface value of dissolved oxygen and $c(\text{O}_2)_{\text{sat}}$ is the saturation value for the surface temperature and salinity.

The exchange of dissolved oxygen between the atmosphere and ocean will be affected by the presence of sea ice. Recent laboratory experiments showed that in sea ice cover of 85%, the gas transfer velocity was reduced to just 25% of its original value (Loose et al. 2009). This reduction is used in the mPWP model when sea ice is present.

2) BIOLOGICAL PROCESSES

Previous studies using PWP have used biological fluxes estimated from Argo floats to construct a net community production (NCP) profile of the water column (Martz et al. 2008). A negative NCP rate indicates respiration is higher than productivity, and so the overall dissolved oxygen concentration will decrease. This profile can then be applied at each time step, reducing (or increasing) the dissolved oxygen concentration by the NCP that occurred during that time.

Respiration rates are rarely measured or reported, especially for the subsurface ocean. The model would benefit from further development to improve this, as well as additional measurements of $c(\text{O}_2)$ and

chlorofluorocarbon (CFC) or sulfur hexafluoride (SF₆) concentrations from the Amundsen Sea region in order to calculate respiration rates at depth. Instead, the NCP profile for this model is estimated based on the [Martz et al. \(2008\)](#) study in the South Pacific.

The surface values of NCP are approximately 15–20 times smaller than those reported by [Ducklow et al. \(2015\)](#). Initial runs did use NCP values an order of magnitude greater (increasing both net production at the surface and net respiration at depth), but the effects of the respiration at depth were too great and resulted in a significant depletion of dissolved oxygen. This is likely due to the limitations associated with a one-dimensional model, where parameterizations of processes such as eddy diffusivity and advection may be not be sufficient for modeling dissolved oxygen concentrations over a long period of time. To temporarily fix this, the NCP rates discussed above were used, resulting in only slightly depleted dissolved oxygen concentrations at depth after the 10-yr model run.

Biological productivity—and to a lesser extent respiration—will have a distinct seasonal cycle, as the phytoplankton and bacteria will be affected by light levels, availability of nutrients, and water temperature. Ideally, in order to model this, time series data of oxygen and respiration rates (using CFC or SF₆ as tracers) below the mixed layer are required. As this information is currently lacking for the Amundsen Sea, no changes are made to the net respiration portion of the curve throughout the year. Through the austral winter, there is no sunlight and therefore no productivity can occur. The region of the water column where net productivity occurs in the summer is instead set to the maximum respiration rates during periods when shortwave radiation is zero.

REFERENCES

- Assmann, K. M., A. Jenkins, D. R. Shoosmith, D. P. Walker, S. S. Jacobs, and K. W. Nicholls, 2013: Variability of circumpolar deep water transport onto the Amundsen Sea continental shelf through a shelf break trough. *J. Geophys. Res. Oceans*, **118**, 6603–6620, doi:10.1002/2013JC008871.
- Bamber, J. L., R. E. Riva, B. L. Vermeersen, and A. M. LeBrocq, 2009: Reassessment of the potential of the West Antarctic ice sheet. *Science*, **324**, 901–903, doi:10.1126/science.1169335.
- Beard, N., F. Straneo, and W. Jenkins, 2015: Spreading of Greenland meltwaters in the ocean revealed by noble gases. *Geophys. Res. Lett.*, **42**, 7705–7713, doi:10.1002/2015GL065003.
- Chen, D., L. M. Rothstein, and A. J. Busalacchi, 1994: A hybrid vertical mixing scheme and its application to tropical ocean models. *J. Phys. Oceanogr.*, **24**, 2156–2179, doi:10.1175/1520-0485(1994)024<2156:AHVMSA>2.0.CO;2.
- Ducklow, H. W., and Coauthors, 2015: Particle flux on the continental shelf in the Amundsen Sea Polynya and Western Antarctic Peninsula. *Elementa Sci. Anthropocene*, **3**, 46, doi:10.12952/journal.elementa.000046.
- Dutrieux, P., and Coauthors, 2014: Strong sensitivity of Pine Island ice-shelf melting to climatic variability. *Science*, **343**, 174–178, doi:10.1126/science.1244341.
- Fofonoff, N., and R. Millard, 1983: Algorithms for computation of fundamental properties of seawater. UNESCO Tech. Paper in Marine Science 44, 58 pp. [Available online at <http://unesdoc.unesco.org/images/0005/000598/059832eb.pdf>.]
- Greenbaum, J. S., and Coauthors, 2015: Ocean access to a cavity beneath Totten Glacier in East Antarctica. *Nat. Geosci.*, **8**, 294–298, doi:10.1038/ngeo2388.
- Heywood, K., and Coauthors, 2016: Between the devil and the deep blue sea: The role of the Amundsen Sea continental shelf in exchanges between ocean and ice shelves. *Oceanography*, **29** (4), 118–129, doi:10.5670/oceanog.2016.104.
- IOC, SCOR, and IAPSO, 2010: The international thermodynamic equation of seawater–2010: Calculation and use of thermodynamic properties. IOC Manuals and Guides 56, UNESCO, 196 pp. [Available online at <http://unesdoc.unesco.org/images/0018/001881/188170e.pdf>.]
- IPCC, 2014: *Climate Change 2014: Impacts, Adaptation, and Vulnerability. Part A: Global and Sectoral Aspects*. Cambridge University Press, 1132 pp.
- Jacobs, S. S., and C. F. Giulivi, 2010: Large multidecadal salinity trends near the Pacific–Antarctic continental margin. *J. Climate*, **23**, 4508–4524, doi:10.1175/2010JCLI3284.1.
- , H. H. Hellmer, and A. Jenkins, 1996: Antarctic ice sheet melting in the southeast Pacific. *Geophys. Res. Lett.*, **23**, 957–960, doi:10.1029/96GL00723.
- , A. Jenkins, C. F. Giulivi, and P. Dutrieux, 2011: Stronger ocean circulation and increased melting under Pine Island Glacier ice shelf. *Nat. Geosci.*, **4**, 519–523, doi:10.1038/ngeo1188.
- , —, H. Hellmer, C. Giulivi, F. Nitsche, B. Huber, and R. Guerrero, 2012: The Amundsen Sea and the Antarctic Ice Sheet. *Oceanography*, **25** (3), 154–163, doi:10.5670/oceanog.2012.90.
- Jenkins, A., 1999: The impact of melting ice on ocean waters. *J. Phys. Oceanogr.*, **29**, 2370–2381, doi:10.1175/1520-0485(1999)029<2370:TIOMIO>2.0.CO;2.
- , and S. Jacobs, 2008: Circulation and melting beneath George VI Ice Shelf, Antarctica. *J. Geophys. Res.*, **113**, C04013, doi:10.1029/2007JC004449.
- , P. Dutrieux, S. Jacobs, S. D. McPhail, J. R. Perrett, A. T. Webb, and D. White, 2010: Observations beneath Pine Island Glacier in West Antarctica and implications for its retreat. *Nat. Geosci.*, **3**, 468–472, doi:10.1038/ngeo890.
- , —, —, S. Mcphail, J. Perrett, A. Webb, and D. White, 2012: Autonomous underwater vehicle exploration of the ocean cavity beneath an Antarctic Ice Shelf. *Oceanography*, **25** (3), 202–203, doi:10.5670/oceanog.2012.95.
- , —, —, E. Steig, G. Gudmundsson, J. Smith, and K. Heywood, 2016: Decadal ocean forcing and Antarctic ice sheet response: Lessons from the Amundsen Sea. *Oceanography*, **29** (4), 106–117, doi:10.5670/oceanog.2016.103.
- Joughin, I., B. E. Smith, and B. Medley, 2014: Marine ice sheet collapse potentially under way for the Thwaites Glacier Basin, West Antarctica. *Science*, **344**, 735–739, doi:10.1126/science.1249055.
- Kim, I., D. Hahm, T. S. Rhee, T. W. Kim, C.-S. Kim, and S. Lee, 2016: The distribution of glacial meltwater in the Amundsen Sea, Antarctica, revealed by dissolved helium and neon. *J. Geophys. Res. Oceans*, **121**, 1654–1666, doi:10.1002/2015JC011211.

- Kraus, E. B., and J. S. Turner, 1967: A one-dimensional model of the seasonal thermocline II. The general theory and its consequences. *Tellus*, **19**, 98–106, doi:10.3402/tellusa.v19i1.9753.
- Lazarevich, P., and S. Stoermer, 2001: A Matlab version of the Price, Weller, Pinkel model. Accessed 29 March 2017. [Available online at <http://www.po.gso.uri.edu/rafos/research/pwp/>.]
- , T. Rossby, and C. McNeil, 2004: Oxygen variability in the near-surface waters of the northern North Atlantic: Observations and a model. *J. Mar. Res.*, **62**, 663–683, doi:10.1357/0022240042387547.
- Loose, B., and W. J. Jenkins, 2014: The five stable noble gases are sensitive unambiguous tracers of glacial meltwater. *Geophys. Res. Lett.*, **41**, 2835–2841, doi:10.1002/2013GL058804.
- , W. R. McGillis, P. Schlosser, D. Perovich, and T. Takahashi, 2009: Effects of freezing, growth, and ice cover on gas transport processes in laboratory seawater experiments. *Geophys. Res. Lett.*, **36**, L05603, doi:10.1029/2008GL036318.
- Martz, T. R., K. S. Johnson, and S. C. Riser, 2008: Ocean metabolism observed with oxygen sensors on profiling floats in the South Pacific. *Limnol. Oceanogr.*, **53**, 2094–2111, doi:10.4319/lo.2008.53.5_part_2.2094.
- Nakayama, Y., M. Schröder, and H. Hellmer, 2013: From circumpolar deep water to the glacial meltwater plume on the eastern Amundsen Shelf. *Deep-Sea Res. I*, **77**, 50–62, doi:10.1016/j.dsr.2013.04.001.
- , R. Timmermann, C. B. Rodehacke, M. Schröder, and H. H. Hellmer, 2014: Modeling the spreading of glacial meltwater from the Amundsen and Bellingshausen Seas. *Geophys. Res. Lett.*, **41**, 7942–7949, doi:10.1002/2014GL061600.
- Naveira Garabato, A. C., and Coauthors, 2017: Vigorous lateral export of the meltwater outflow from beneath an Antarctic ice shelf. *Nature*, **542**, 219–222, doi:10.1038/nature20825.
- Niiler, P. P., 1975: Deepening of wind-mixed layer. *J. Mar. Res.*, **33**, 405–422.
- , and E. B. Kraus, 1977: One-dimensional models of the upper ocean. *Modelling and Prediction of the Upper Layers of the Ocean*, E. B. Kraus, Ed., Pergamon, 143–172.
- Orsi, A. H., T. Whitworth, and W. D. Nowlin, 1995: On the meridional extent and fronts of the Antarctic Circumpolar Current. *Deep-Sea Res. I*, **42**, 641–673, doi:10.1016/0967-0637(95)00021-W.
- Paolo, F. S., H. A. Fricker, and L. Padman, 2015: Volume loss from Antarctic ice shelves is accelerating. *Science*, **348**, 327–332, doi:10.1126/science.aaa0940.
- Payne, A. J., A. Vieli, A. P. Shepherd, D. J. Wingham, and E. Rignot, 2004: Recent dramatic thinning of largest West Antarctic ice stream triggered by oceans. *Geophys. Res. Lett.*, **31**, L23401, doi:10.1029/2004GL021284.
- Price, J. F., R. A. Weller, and R. Pinkel, 1986: Diurnal cycling: Observations and models of the upper ocean response to diurnal heating, cooling, and wind mixing. *J. Geophys. Res.*, **91**, 8411–8427, doi:10.1029/JC091iC07p08411.
- Pritchard, H. D., S. R. M. Ligtenberg, H. A. Fricker, D. G. Vaughan, M. R. van den Broeke, and L. Padman, 2012: Antarctic ice-sheet loss driven by basal melting of ice shelves. *Nature*, **484**, 502–505, doi:10.1038/nature10968.
- Randall-Goodwin, E., and Coauthors, 2015: Freshwater distributions and water mass structure in the Amundsen Sea Polynya region, Antarctica. *Elementa Sci. Anthropocene*, **3**, 65, doi:10.12952/journal.elementa.000065.
- Richardson, G., M. R. Wadley, K. J. Heywood, D. P. Stevens, and H. T. Banks, 2005: Short-term climate response to a freshwater pulse in the Southern Ocean. *Geophys. Res. Lett.*, **32**, L03S03, doi:10.1029/2004GL020679.
- Rignot, E., S. Jacobs, J. Mouginot, and B. Scheuchl, 2013: Ice-shelf melting around Antarctica. *Science*, **341**, 266–270, doi:10.1126/science.1235798.
- Saha, S., and Coauthors, 2006: The NCEP Climate Forecast System. *J. Climate*, **19**, 3483–3517, doi:10.1175/JCLI3812.1.
- Schodlok, M. P., D. Menemenlis, E. Rignot, and M. Studinger, 2012: Sensitivity of the ice-shelf/ocean system to the sub-ice-shelf cavity shape measured by NASA IceBridge in Pine Island Glacier, West Antarctica. *Ann. Glaciol.*, **53**, 156–162, doi:10.3189/2012AoG60A073.
- Stammerjohn, S. E., and Coauthors, 2015: Seasonal sea ice changes in the Amundsen Sea, Antarctica, over the period of 1979–2014. *Elementa Sci. Anthropocene*, **3**, 55, doi:10.12952/journal.elementa.000055.
- Thoma, M., A. Jenkins, D. Holland, and S. Jacobs, 2008: Modelling Circumpolar Deep Water intrusions on the Amundsen Sea continental shelf, Antarctica. *Geophys. Res. Lett.*, **35**, L18602, doi:10.1029/2008GL034939.
- Thurnherr, A., S. S. Jacobs, P. Dutrieux, and C. F. Giulivi, 2014: Export and circulation of ice cavity water in Pine Island Bay, West Antarctica. *J. Geophys. Res. Oceans*, **119**, 1754–1764, doi:10.1002/2013JC009307.
- Tomczak, M., 1981: A multi-parameter extension of temperature/salinity diagram techniques for the analysis of non-isopycnal mixing. *Prog. Oceanogr.*, **10**, 147–171, doi:10.1016/0079-6611(81)90010-0.
- , and D. G. B. Large, 1989: Optimum multiparameter analysis of mixing in the thermocline of the eastern Indian Ocean. *J. Geophys. Res.*, **94**, 16 141–16 149, doi:10.1029/JC094iC11p16141.
- Wählin, A. K., and Coauthors., 2013: Variability of warm deep water inflow in a submarine trough on the Amundsen Sea Shelf. *J. Phys. Oceanogr.*, **43**, 2054–2070, doi:10.1175/JPO-D-12-0157.1.
- Walker, D. P., A. Jenkins, K. M. Assmann, D. R. Shoosmith, and M. A. Brandon, 2013: Oceanographic observations at the shelf break of the Amundsen Sea, Antarctica. *J. Geophys. Res. Oceans*, **118**, 2906–2918, doi:10.1002/jgrc.20212.
- Wanninkhof, R., 2014: Relationship between wind speed and gas exchange over the ocean. *Limnol. Oceanogr. Methods*, **12**, 351–362, doi:10.4319/lom.2014.12.351.
- Webber, B., and Coauthors, 2017: Mechanisms driving variability in the ocean forcing of Pine Island Glacier. *Nat. Commun.*, **8**, 14507, doi:10.1038/ncomms14507.